HHS Public Access

Author manuscript

Dev Cell. Author manuscript; available in PMC 2021 August 24.

Published in final edited form as:

Dev Cell. 2020 August 24; 54(4): 455–470.e5. doi:10.1016/j.devcel.2020.05.027.

DDX3X suppresses the susceptibility of hindbrain lineages to medulloblastoma

Deanna M. Patmore[1], **Amir Jassim**[1], **Erica Nathan**[1], **Reuben J. Gilbertson**[1], **Daniel Tahan**[1], **Nadin Hoffmann**[1], **Yiai Tong**[2], **Kyle S. Smith**[2], **Thirumala-Devi Kanneganti**[3], **Hiromichi Suzuki**[4], **Michael D. Taylor**[4], **Paul Northcott**[2], **Richard J. Gilbertson**[1,5,*]

[1]CRUK Cambridge Institute, University of Cambridge, Li Ka Shing Centre, Robinson Way, Cambridge CB2 0RE, England; [2]Department of Developmental Neurobiology, St Jude Children's Research Hospital, 262 Danny Thomas Place, Memphis, TN 38105, USA; [3]Department of Immunology, St Jude Children's Research Hospital, 262 Danny Thomas Place, Memphis, TN 38105, USA; [4]D ivision of Neurosurgery, The Hospital for Sick Children, 555 University Avenue Toronto, Ontario, Canada M5G 1X8 [5]Department of Oncology, University of Cambridge, Li Ka Shing Centre, Robinson Way, Cambridge CB2 0RE, England;

SUMMARY:

DDX3X is frequently mutated in the WNT and SHH subtypes of medulloblastoma - the commonest malignant childhood brain tumor. But whether *DDX3X* functions as a medulloblastoma oncogene or tumor suppressor gene is not known. Here, we show that *Ddx3x* regulates hindbrain patterning and development by controlling *Hox* gene expression and cell stress signaling. In mice predisposed to Wnt or Shh-medulloblastoma, *Ddx3x* sensed oncogenic stress and suppressed tumor formation. WNT and SHH-medulloblastomas normally arise only in the lower and upper rhombic lips, respectively. Deletion of *Ddx3x* removed this lineage restriction, enabling both medulloblastoma subtypes to arise in either germinal zone. Thus, *DDX3X* is a medulloblastoma tumor suppressor that regulates hindbrain development and restricts the competence of cell lineages to form medulloblastoma subtypes.

Graphical Abstract

Correspondence should be addressed to RJG: Richard.Gilbertson@cruk.cam.ac.uk.

AUTHOR CONTRIBUTIONS

D.M.P. was involved in much of the methodology, investigation, formal analysis and data visualization. E.N., A.J., R.G., D.T., N.H., Y.T., K.S.S., were involved in investigation and formal analysis. P.A.N., and M.D.T., were involved in methodology, supervision and providing resources. T-D.K., was involved in writing and providing resources. R.J.G., was responsible for conceptualization of the study, methodology, formal analysis, writing the original draft, data visualization, supervision and funding acquisition.

*lead author

DECLARATION OF INTERESTS

None

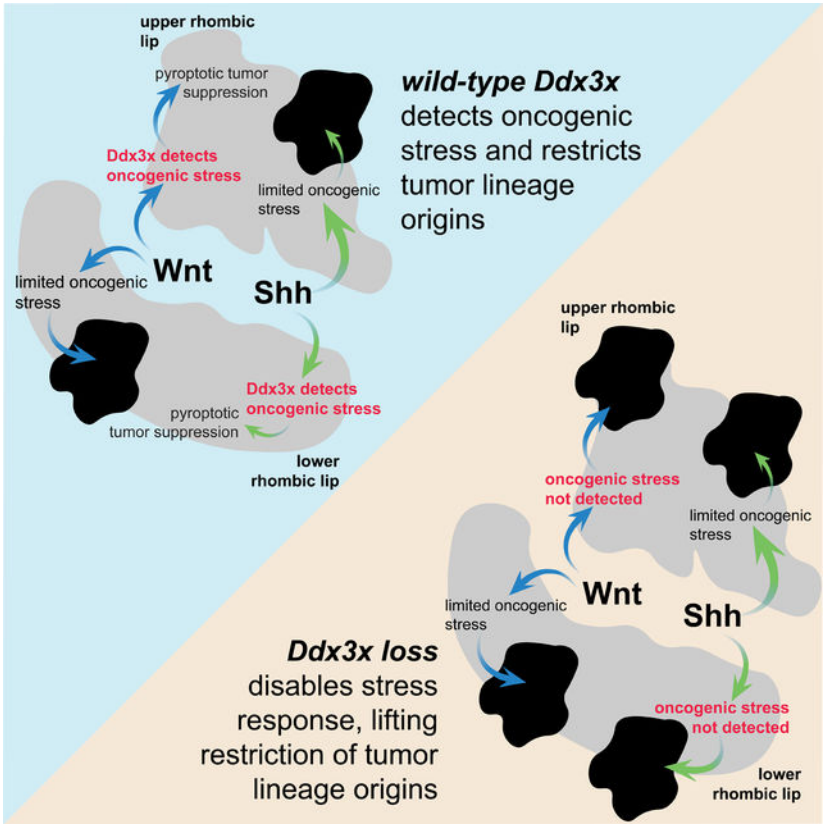

eTOC

DDX3X is frequently mutated in medulloblastoma - a common childhood hindbrain tumor. Patmore et al., show that *Ddx3x* regulates hindbrain development and suppresses medulloblastoma formation by controlling *Hox* gene expression, cell stress signaling and restricting the number of cell lineages that can form tumors.

Keywords

medulloblastoma; tumor suppressor gene; DDX3X; inflammasome; stress granule

INTRODUCTION

Genome-wide studies of cancer have transformed our understanding of the disease. Taxonomies based solely on tumor location and histology have evolved into more precise classifications that include details of the cancer transcriptome, methylome and mutational landscape (Doherty et al., 2019; Roychowdhury and Chinnaiyan, 2014). The hope is that this molecular revolution will usher in a new era of precision cancer medicine that ultimately improves patient outcome. But early successes in leukemia have proved hard to replicate in other malignancies (Druker et al., 2001; Letai, 2017). A deeper understanding of the functional consequences of genomic-aberrations is likely to be required if we are to fully realize the promise of precision medicine for all patients with cancer.

The challenge of translating genomic understanding into patient cures is well illustrated by medulloblastoma - the commonest malignant childhood brain tumor. Once considered a single disease, medulloblastoma is now known to comprise at least four subtypes, each with distinct origins, genomic drivers and clinical outcomes (Northcott et al., 2019): SHH-medulloblastomas arise from cerebellar granule neuron precursor cells (NPCs), contain activating mutations in the SHH pathway, and are fatal in ~25% of cases; Group 3-medulloblastomas likely arise from Nestin^{+} cerebellar NPCs, amplify *MYC* in 17% of cases, and kill around half of all patients; while Group 4 medulloblastomas probably arise within the cerebellar unipolar brush cell lineage, contain more complex genetic drivers and are fatal in ~25% of cases (Hovestadt et al., 2019; Jones et al., 2012; Kawauchi et al., 2012; Northcott et al., 2012b; Pugh et al., 2012; Robinson et al., 2012; Vladoiu et al., 2019; Yang et al., 2008). In stark contrast, WNT-medulloblastomas arise from mossy fiber NPCs in the lower rhombic lip, are curable even when metastatic, and frequently contain activating mutations in *CTNNB1* (Gajjar et al., 2006; Gibson et al., 2010; Jessa et al., 2019; Northcott et al., 2012a; Northcott et al., 2011). While this knowledge has enabled more accurate prediction of patient prognosis and use of conventional treatment, it is yet to yield novel curative therapies. Achieving this will require an understanding of how genomic patterns are laid down and function in medulloblastoma, and in particular why specific driver mutations are exquisitely restricted to each tumor subtype.

The discovery that *DDX3X* - an RNA-binding protein of the DEAD-box family - is frequently mutated in WNT- (36%) and SHH- (21%) but not Group 3- or 4-medulloblastomas, provides an inroad to understand the functional basis of medulloblastoma subtypes (Jones et al., 2012; Northcott et al., 2012b; Pugh et al., 2012; Robinson et al., 2012). Therefore, we studied the role of *DDX3X* in hindbrain development and medulloblastoma tumorigenesis.

RESULTS

Ddx3x regulates hindbrain development

As a first step to understand the role of *Ddx3x* in health and disease, we generated a conditional knock-out allele (*Ddx3x*^{Flx}) by inserting LoxP sites into introns 6 and 14 (Samir et al., 2019). Since *Ddx3x* is located on chromosome X, Cre-recombination of *Ddx3x*^{Flx} led to the complete loss of Ddx3x protein from female *Ddx3x*$^{Flx/Flx}$ and male *Ddx3x*$^{Flx/Y}$ NPCs, and a ~50% reduction of expression in female *Ddx3x*$^{Flx/+}$ NPCs (Figure 1A).

Mice harboring *Ddx3x*^{Flx} were bred with those carrying the *Blbp-Cre* allele that drives Cre-recombination from embryonic day (E) 9.5 in NPCs throughout the neuroaxis, including lower and upper rhombic lip NPCs that are competent to form Wnt- and Shh-medulloblastomas, respectively (Gibson et al., 2010). Thirty-eight percent (n=21/55) of female *Blbp-Cre*$^{+/-}$;*Ddx3x*$^{Flx/Flx}$ mice displayed severe ataxia and seizures within 34 days of life (Figure 1B). Growth of all brain regions, especially the cerebellum, was significantly impaired in these animals relative to *Blbp-Cre*$^{+/-}$;*Ddx3x*$^{+/+}$ control mice (≥10 mice per time point; Figure 1C) and was associated with induction of apoptosis (cleaved Caspase 3), cell cycle arrest (p21), and/or loss of total cell number (Figure 1C; Figure S1A). *Blbp-Cre*$^{+/-}$;*Ddx3x*$^{Flx/Flx}$ mice had morphologically normal cerebella at E16.5 but subsequently

displayed progressive abnormalities of both upper and lower rhombic lip-derived cell lineages, including: loss of normal cerebellar foliation and lamination (Figure 1D–F); failure of formation of major brainstem nuclei (Figure S1B); collections of abnormal 'rests' of proliferating Atoh1^{+}/Pax6^{+}/Ki67^{+} cerebellar granule NPCs intermingled within sheets of Synaptophysin^{+} neurons (Figure 1G and H); disorganization of the normal Gfap^{+} Bergman glia radial scaffold (Figure 1H); and haphazard positioning of Calbindin^{+} Purkinje cells (Figure 1H). Brain growth and cell organization were also disrupted in *Blbp-Cre*$^{+/-}$;*Ddx3x*$^{Flx/Flx}$ mice that survived into adulthood, albeit to a lesser extent than those displaying neurological impairment (data not shown). In contrast, neither *Blbp-Cre*$^{+/-}$;*Ddx3x*$^{Flx/+}$ female (n=29; median follow-up=101 days) nor *Blbp-Cre*$^{+/-}$;*Ddx3x*$^{Flx/Y}$ male mice (n=31; median follow-up=182 days) displayed neurological, brain size or cell organization abnormalities; although the total number of cells throughout the brains of these mice was reduced at P30, suggesting that loss of *Ddx3x* is not compensated for completely in these animals (Figure 1B–H).

Thus, *Ddx3x* specifies and/or maintains hindbrain lineages, including those that generate Wnt and Shhmedulloblastoma. Although *Ddx3x* expression is ablated completely in NPCs of *Blbp-Cre*$^{+/-}$;*Ddx3x*$^{Flx/Y}$ male mice (Figure 1A), these mice developed relatively normally; therefore, the paralog *Ddx3y* likely compensates for *Ddx3x* during development in a manner similar to that of other paralog pairs (Welstead et al., 2012). In keeping with this notion, *Ddx3y* was upregulated in *Blbp-Cre*$^{+/-}$;*Ddx3x*$^{Flx/Y}$ hindbrains relative to male *Blbp-Cre*$^{+/-}$;*Ddx3x*$^{+/+}$ controls (P13 and P30 $P<0.05$; Figure 1I).

Ddx3x regulates hindbrain patterning and stress response

Hindbrain development involves a highly-orchestrated program of regional gene expression. Central to this process are the *Hox* genes that govern the formation of distinct rhombomeres (Kiecker and Lumsden, 2005). Since Ddx3x regulates global patterns of gene expression, including the *Hox* genes, we looked to see if *Hox* expression is perturbed in the hindbrain following *Ddx3x* deletion (Duijkers et al., 2019; Herdy et al., 2018; Valentin-Vega et al., 2016).

Global patterns of gene expression among developing *Blbp-Cre*$^{+/-}$;*Ddx3x*$^{+/+}$, *Blbp-Cre*$^{+/-}$;*Ddx3x*$^{Flx/+}$, *Blbp-Cre*$^{+/-}$;*Ddx3x*$^{Flx/Y}$ and *Blbp-Cre*$^{+/-}$;*Ddx3x*$^{Flx/Flx}$ hindbrains were dictated predominantly by developmental stage rather than genotype (≥5 hindbrains per timepoint and genotype; Figure 2A). However at E16.5, 0.08% (27/32,075) and 0.12% (38/32,075) of all RNA transcripts were upregulated and downregulated respectively in *Blbp-Cre*$^{+/-}$;*Ddx3x*$^{Flx/Flx}$ hindbrains relative to age matched *Blbp-Cre*$^{+/-}$;*Ddx3x*$^{+/+}$ controls (Figure 2B). Expression of these genes was not affected in *Blbp-Cre*$^{+/-}$;*Ddx3x*$^{Flx/+}$ or *Blbp-Cre*$^{+/-}$;*Ddx3x*$^{Flx/Y}$ hindbrains. Remarkably, 58% (22/38) of downregulated genes are Homeobox genes (FDR=3.2e^{-23}), including: *Gbx1* that specifies the midbrain-hindbrain boundary; *Pax2* and *Gbx2* (primordial cerebellum); *Hoxa2* (rhombomere 2); *Hoxb2* (rhombomere 3); *Hoxa3* and *Hoxb3* (rhombomeres 5 and 6); *Hoxa4* and *Hoxb4* (rhombomere 7); and *Phox2b, Tbx20*, and *Nkx6–1* (regulators of developmental gene transcription; Figure 2B). Pathway analysis of all dysregulated genes using g:GOST within the g:Profiler interface (Raudvere et al., 2019) and Cytoscape algorithms (Shannon et al.,

2003) confirmed enrichment for regulators of neuronal development (n=42 related pathways; FDR=4.7e^{-2} to 3.2e^{-23}), RNA processing and transcription (n=11 related pathways; FDR=1.1e^{-3} to 6.9e^{-9}), cranial nerve development (n=3 related pathways; FDR=2.8e^{-5} to 2.0e^{-7}) and cell motility (n=1 related pathway; FDR=3.8e^{-2}; Figure 2B). By P5, *Blbp-Cre*$^{+/-}$;*Ddx3x*$^{Flx/Flx}$ hindbrains also expressed lower levels of neural fate commitment genes including *Ascl1, Kirrel2, Lhx5, Neurog1, Neurog2* and *Pax2* that mark cerebellar ventricular zone NPCs and GABAergic lineages (Figure 2B): *Lhx5* is a known Hox target gene (Makki and Capecchi, 2011). These data suggest strongly that *Ddx3x* regulates early hindbrain development by directly, or indirectly, regulating *Hox* gene expression and that *Ddx3y* compensates for *Ddx3x* loss during development, at least in part, by maintaining *Hox* expression.

We showed previously that Ddx3x shuttles between stress granules and NLRP3-inflammasomes to coordinate live-or-die decisions in response to cell stress (Samir et al., 2019). Incorporation of Ddx3x into stress granules promotes a cell survival signal, while its inclusion in inflammasomes drives pyroptosis - a form of programmed cell death important in the innate immune response and neurodegeneration (McKenzie et al., 2019a; Voet et al., 2019). In keeping with this function, P13 *Blbp-Cre*$^{+/-}$;*Ddx3x*$^{Flx/Flx}$ hindbrains dysregulated inflammasome (FDR=1.1e^{-6}), cell stress (n=2 related pathways; FDR=1.1e^{-4} to 1.0e^{-6}), immune (n=16 related pathways; FDR=0.05 to 6.0e^{-5}) and apoptotic response regulators (n=5 related pathways; FDR=0.01 to 5.6e^{-5}; Figure 2B). Histological review demonstrated that this response was triggered in neuronal cells rather than representing a significant infiltration of immune cells or expansion of resident microglia (Figure S2). Thus, aberrant development of the postnatal *Blbp-Cre*$^{+/-}$;*Ddx3x*$^{Flx/Flx}$ hindbrain might be exacerbated by deregulation of stress granule-inflammasome signaling in neuronal cells in a manner similar to that reported in neurodegenerative conditions (McKenzie et al., 2019a; Voet et al., 2019). No such response was observed in *Blbp-Cre*$^{+/-}$;*Ddx3x*$^{Flx/Y}$ mice despite the fact that *Ddx3y* does not compensate for the stress signaling functions of *Ddx3x* (Samir et al., 2019). Therefore, we propose that abnormal development of the embryonic *Blbp-Cre*$^{+/-}$;*Ddx3x*$^{Flx/Flx}$ hindbrain, rather than deletion of *Ddx3x per se*, triggers stress signals to which these mice are unable to respond appropriately.

Ddx3x is a medulloblastoma tumor suppressor gene

We next sought to understand the role of *DDX3X* in medulloblastoma. WNT and SHH pathway mutations are found almost exclusively in WNT and SHH-medulloblastomas respectively, while mutations in *DDX3X* occur frequently in both of these tumor subtypes (Northcott et al., 2019). The molecular basis of this subtype-specific distribution of mutations and whether *DDX3X* is a medulloblastoma oncogene or tumor suppressor gene is not known. Therefore, we recorded patterns of tumor formation in mice harboring the *Ddx3x*^{Flx} allele that were predisposed to develop either Wnt- (*Blbp-Cre*$^{+/-}$;*Ctnnb1*$^{Flx/+}$;*Tp53*$^{Flx/+}$, hereon *mWnt*) or Shh-medulloblastoma (*Blbp-Cre*$^{+/-}$;*Ptch1*$^{Flx/+}$, hereon *mShh*).

As expected (Gibson et al., 2010), 7% (n=4/55, median surveillance=145 days) of *mWnt;Ddx3x*$^{+/+}$ mice developed medulloblastomas embedded in the brainstem with no

evidence of transformation in the cerebellum (Figure 3A, C and H). *mWnt;Ddx3x*$^{Flx/+}$ mice also developed tumors exclusively from the dorsal brainstem with a similar incidence and latency (Figure 3A and H). In stark contrast, 27% (n=13/47) of *mWnt;Ddx3x*$^{Flx/Y}$ and 7% (n=3/44) of *mWnt;Ddx3x*$^{Flx/Flx}$ mice developed tumors that were confined solely to the cerebellum with no evidence of tumorigenesis in the brainstem - presumably because of the longer latency of brainstem relative to cerebella tumorigenesis. Tumors in these mice ranged from a diffuse expansion of the external granule cell layer to discrete tumor masses (Figure 3D and E). Both comprised highly proliferative, Pax6^{+}/Ki67^{+}/Atoh1^{+}/Lef1^{+} small round blue cells, compatible with mutant *Ctnnb1*-driven transformation of granule NPCs. Notably, nuclear G3bp1 expression that has been associated with cell stress (Tourrière et al., 2001) was particularly upregulated in cerebellar *mWnt;Ddx3x*$^{Flx/Y}$ medulloblastomas (Figure 3D).

Remarkably, *Ddx3x* also suppressed both the prevalence and distribution of *mShh* tumors. Twenty-six percent (n=23/87) of *mShh;Ddx3x*$^{+/+}$ mice developed tumors that were confined solely to the cerebellum (Figure 3B, F and I). Medulloblastomas also formed exclusively in the cerebella of *mShh;Ddx3x*$^{Flx/+}$ mice, although with a significantly greater prevalence and reduced latency (45%, n=17/38; prevalence, P=0.04; survival Log Rank, P<0.05; Figures 3B and I). In contrast, of the 50% (n=19/38) of *mShh;Ddx3x*$^{Flx/Y}$ mice that developed tumors, more than half arose in the brainstem (Figure 3B and I). In two mice these tumors were confined solely to the brainstem, while eight arose simultaneously in the brainstem and cerebellum. Of the 18% (n=3/17) of *mShh;Ddx3x*$^{Flx/Flx}$ mice that developed tumors, two occurred simultaneously in the cerebellum and brainstem (Figure B, G and I). *mShh;Ddx3x*$^{+/+}$ and *mShh;Ddx3x*$^{Flx/Y}$ cerebella tumors preserved the locus and expression of the wild-type *Ptch1* allele, in keeping with reports the *Ptch1* serve as a haploinsufficient suppressor of medulloblastoma (Wetmore et al., 2000) (Figure S3). All *mShh* tumors, including those in the brainstem, were Lef1^{-} distinguishing them from tumors driven by activation of *Ctnnb1* (Figure 3G). Similar to the development of *mWnt* tumors, the prevalence and location of *mShh* tumors were impacted most significantly in male *Ddx3x*$^{Flx/Y}$ mice (Figure 3B and I).

WNT-medulloblastomas have not been reported to arise in the cerebellum nor SHH-medulloblastomas in the brainstem, suggesting that *Ddx3x* restricts the competence of cell lineages to form these tumor subtypes. However, it is also possible that these tumors had spread directly, or metastatically, from their more recognized origins. Therefore, we sought additional evidence that *mWnt;Ddx3x*$^{Flx/Y}$ cerebellar tumors are distinct from those in the brainstem of *mWnt;Ddx3x*$^{+/+}$ mice (we were unable to isolate adequate material for further analysis from *mShh;Ddx3x*$^{Flx/Y}$ or *mShh;Ddx3x*$^{Flx/Flx}$ brainstem, or *mWnt;Ddx3x*$^{Flx/Flx}$ cerebellar tumors). RNAseq analysis identified three very discrete groups of tumors: (i) all *mShh* cerebellar tumors regardless of *Ddx3x* genotype; (ii) *mWnt;Ddx3x*$^{+/+}$ brainstem tumors; and (iii) *mWnt;Ddx3x*$^{Flx/Y}$ cerebellar tumors (Figure 4 A and B). As expected, *mWnt;Ddx3x*$^{+/+}$ brainstem and all *mShh* cerebellar tumors recapitulated the gene expression signatures of their corresponding human medulloblastoma subtypes (Gibson *et. al.*, 2010; Figure 4B). In keeping with their high-expression of Lef1, *mWnt;Ddx3x*$^{Flx/Y}$ tumors also displayed a human WNT-medulloblastoma signature (Figure 4B); however, in contrast to *mWnt;Ddx3x*$^{+/+}$ brainstem tumors, *mWnt;Ddx3x*$^{Flx/Y}$ tumors potently upregulated cell cycle (n=34 related pathways; FDR=0.02 to 2.8e^{-44}), immune (n=23 related pathways; FDR=0.04 to 9.0e^{-07}), cell stress (n=4 related pathways; FDR=0.02 to 2.0e^{-19}) and death

response genes (n=18 related pathways; FDR=0.02 to $3.2e^{-7}$; Figure 4B and C). This pattern of gene expression was similar to that observed in the developing *Blbp-Cre*$^{+/-}$*;Ddx3x*$^{Flx/Flx}$ hindbrain (Figure 2B). The transcriptome of *mWnt;Ddx3x*$^{Flx/Y}$ (and all *mShh*) cerebellar tumors was also distinguished from that of *mWnt;Ddx3x*$^{+/+}$ brainstem tumors by upregulation of genes expressed by cerebellar granule NPCs and DNA repair pathways (n=11 related pathways; FDR=$7.2e^{-4}$ to $1.6e^{-29}$) that are recognized features of human and mouse cerebella-derived medulloblastomas (Ratnaparkhe et al., 2018).

To provide further evidence that the genomes of *mWnt;Ddx3x*$^{Flx/Y}$ cerebellar and *mWnt;Ddx3x*$^{+/+}$ brainstem tumors are distinct, we performed shallow whole exome sequencing of DNA isolated from these tumors. Both analyzed *mWnt;Ddx3x*$^{Flx/Y}$ cerebella tumors, but neither the *mWnt;Ddx3x*$^{+/+}$ brainstem nor two *mShh;Ddx3x*$^{+/+}$ cerebella tumors, deleted a common region of 7qB3 (Figure S4). Conversely, gain of 6qA1–6qB3 and 18qA1–18qE4 and deletion of 17qE2–17qter were observed only in the *mWnt;Ddx3x*$^{+/+}$ brainstem tumor but no mWnt or mShh cerebella tumors.

Finally, to determine directly if *mWnt;Ddx3x*$^{Flx/Y}$ cerebella can generate tumors, we isolated single cell suspensions from these tissues at P13 - prior to discernable tumor formation (n=12, dissected carefully away from the brainstem) - as well as P13 *mWnt;Ddx3x*$^{+/+}$ (n=5), *mWnt;Ddx3x*$^{Flx/Flx}$ (n=3), *Blbp*$^{+/-}$;*Ddx3x*$^{+/+}$ (n=3), *Blbp*$^{+/-}$;*Ddx3x*$^{Flx/+}$ (n=3), *Blbp*$^{+/-}$;*Ddx3x*$^{Flx/Y}$ (n=3), and *Blbp*$^{+/-}$;*Ddx3x*$^{Flx/Flx}$ (n=3) cerebella. Cell suspensions were transduced with lentiviral-luciferase and 5×10^5 cells injected orthotopically into the cerebella of separate P28 immunocompromised mice as described previously (Mohankumar et al., 2015). Ki67$^+$/Lef1$^+$ tumors formed rapidly in all mice engrafted with *mWnt;Ddx3x*$^{Flx/Y}$ cells (Figures 4D and E). No other engrafted cell types formed tumors, including those from *mWnt;Ddx3x*$^{+/+}$ cerebella that never formed tumors *de novo* or *mWnt;Ddx3x*$^{Flx/Flx}$ cerebella that formed tumors with very low penetrance (Figure 3H; median follow up 90 days).

Thus, *Ddx3x* suppresses the penetrance and restricts lineage origins of *mWnt* and likely *mShh*medulloblastomas, providing a potential explanation why the gene is mutated in both of these tumor subtypes in humans. Since tumor formation was most penetrant in *mWnt;Ddx3x*$^{Flx/Y}$ and *mShh;Ddx3x*$^{Flx/Y}$ mice, then in contrast to its development functions, *Ddx3y* does not compensate for the tumor suppressor function of *Ddx3x*.

Ddx3x suppresses oncogenic Wnt-signaling in the cerebellum

To understand how *Ddx3x* might restrict cell lineage susceptibility to medulloblastoma tumorigenesis, we observed the impact of oncogenic signaling in developing *mWnt* (E16.5-P13) and *mShh* (E16.5-P30) *Ddx3x*$^{+/+}$, *Ddx3x*$^{Flx/+}$, *Ddx3x*$^{Flx/Y}$ and *Ddx3x*$^{Flx/Flx}$ cerebella relative to age-matched *Blbp-Cre;Ddx3x*$^{+/+}$ controls prior to any evidence of tumor formation (≥5 cerebellar/genotype/time point). Global patterns of gene expression in the cerebella of these animals was dictated largely by developmental stage rather than genotype. However, all *mWnt* cerebella, including *mWnt;Ddx3x*$^{+/+}$ and *mWnt;Ddx3x*$^{Flx/+}$ that do not form tumors, displayed aberrant and robust Wnt-signaling that increased with development (Figure 5A,B). Thus, the absence of tumorigenesis in *mWnt;Ddx3x*$^{+/+}$ and *mWnt;Ddx3x*$^{Flx/+}$ cerebella does not result from an inability of these tissues to support

aberrant Wnt signaling. Conversely, no *mWnt* cerebella, including *mWnt;Ddx3x*$^{Flx/Y}$ and *mWnt;Ddx3x*$^{Flx/Flx}$ that form tumors, displayed aberrant Shh-signaling. Thus, the formation of tumors in *mWnt;Ddx3x*$^{Flx/Y}$ and *mWnt;Ddx3x*$^{Flx/Flx}$ cerebella is unlikely to result from oncogenic Shh-signaling (Figures 5A and B).

Rather, compatible with an oncogenic-stress response, Wnt-signaling triggered a profound and progressive activation of cell stress (P13, FDR=8.7e^{-4} to 2.3e^{-10}) cell death (P13, FDR=0.04 to 2.7e^{-9}) and upregulation of p21 and cleaved Caspase 3 in *mWnt;Ddx3x*$^{+/+}$ and *mWnt; Ddx3x*$^{Flx/+}$ cerebella: DNA repair (P5, FDR=1.8e^{-12}), cell cycle progression (P5, FDR=1.2e^{-7} to 1.5e^{-57}) and cell proliferation (Ki67) were down-regulated concurrently in these mice (Figure 5A–F). In stark contrast, deletion of *Ddx3x* blunted *mWnt*-induced cell stress (P13, FDR=0.04 to 1.1e^{-6}) and cell death (P13, FDR=0.01 to 0.003) markedly in *mWnt;Ddx3x*$^{Flx/Y}$ cerebella and neither pathway was induced in *mWnt;Ddx3x*$^{Flx/Flx}$ cerebella (Figure 5B). Furthermore, neither *mWnt;Ddx3x*$^{Flx/Y}$ nor *mWnt;Ddx3x*$^{Flx/Flx}$ cerebella downregulated DNA repair or cell cycle progression pathways and by P13 displayed normal levels Ki67, p21 and cleaved Caspase 3 (Figure 5C–E). Together, these data support the notion that aberrant Wnt signaling in the developing cerebellum provokes a potent oncogenic-stress response mediated by *Ddx3x* to suppress medulloblastoma tumorigenesis. Deletion of *Ddx3x* partially relieves this oncogenic-stress, enabling Wnt-driven malignant transformation. We are investigating if a reciprocal mechanism suppresses oncogenic Shh-signaling in the lower rhombic lip.

In contrast, aberrant Shh-signaling activated cell cycle progression, DNA repair, cell proliferation (Ki67) and a robust SHH-medulloblastoma signature (FDR=1.7e^{-5} to 3.5e^{-5}) with minimal impact on p21 and cleaved Caspase 3 expression in all *mShh* cerebella, regardless of *Ddx3x* genotype, in keeping with the uniform transformation of these tissues (Figures 3I and 5A–F). These data support the notion that Shh signaling - the native mitogen for granule NPCs - is relatively well tolerated by the granule lineage, leading to unopposed transformation independent of *Ddx3x* status. Upregulation of cell cycle progression, DNA repair genes and cell proliferation (Ki67) was much less robust in *mShh;Ddx3x*$^{Flx/Flx}$ cerebella compatible with the relatively low level of tumorigenesis in these tissues (Figures 3I and 5B,C).

Stress signaling in DDX3X mutant human WNT-medulloblastomas

As a first step to determine if deletion of *Ddx3x* in mouse *mWnt*-medulloblastoma is functionally equivalent to mutation of the gene in human WNT-medulloblastoma, we compared single cell RNAseq (scRNAseq) profiles of *DDX3X* mutant (*DDX3X*^{mut}, n=2) and wild-type (*DDX3X*^{wt}, n=3) human WNT-medulloblastomas (Hovestadt et al., 2019). As expected, overall Uniform Manifold Approximation and Projection (UMAP) analysis of scRNAseq profiles segregated WNT-medulloblastoma cells according to the originating tumor/patient (Figure 6A). Therefore, to identify genes that might be dysregulated by mutation of *DDX3X* in WNT-medulloblastoma, we compared gene expression patterns in all cells derived from the two *DDX3X*^{mut} WNT-medulloblastomas (n=766 cells) with those in the three *DDX3X*^{wt} WNT-medulloblastomas (n=1,344 cells; Figure 6B). Remarkably, similar to our comparison of *mWnt;Ddx3x*$^{Flx/Y}$ and *mWnt;Ddx3x*$^{+/+}$ mouse tumors (Figure

4B and C) genes upregulated in *DDX3X*^{mut} versus *DDX3X*^{wt} WNT-medulloblastoma cells were highly enriched for 'stress granule associated' (FDR=2.5e-38 - the most significantly upregulated specific cell function geneset), 'stress response' (FDR=2.2e-20), cell death/apoptosis (FDR=3.1e-8), and DNA repair genes (FDR=8.5e-8; Figure 6B). Several of these genes were commonly upregulated in both mouse *mWNT;Ddx3x*$^{Flx/Y}$ and human *DDX3X*^{mut} WNT-medulloblastoma and are implicated in other neurological disorders, including (Figure 4B, 6B): *ANXA11* that regulates stress granule transport and is disrupted in amyotrophic lateral sclerosis (Liao et al., 2019); *EPCAM, DLX1, FOXB1, IGFBP3, SLIT3, DDX20* that mediate cell death and apoptosis, particularly in neuronal tissues (Dai et al., 2017; Forones et al., 2018; Weber et al., 2018; Zhang et al., 2006); and the DNA repair enzymes *RAD51* and *RAD54L* that are critically upregulated in other brain tumors (McKenzie et al., 2019b; Tong et al., 2015). Intriguingly, human *DDX3X*^{mut} WNT-medulloblastoma cells also upregulated cerebellar granule NPC markers, including *NEUROD1, PAX6, ATAD2* and *BAZ1A* that were upregulated in *mWnt;Ddx3x*$^{Flx/Y}$ mouse cerebellar tumors (FDR=1.0e-4; Figure 4B and 6B). Thus, as suggested by recent imaging of human tumors (Di Giannatale et al., 2016), a small fraction of human *DDX3X*^{mut} WNT-medulloblastomas might arise within the cerebellar granule NPC lineage.

Finally, analysis of bulk RNAseq profiles generated from a separate cohort of human *DDX3X*^{mut} (n=14) and *DDX3X*^{wt} (n=14) WNT-medulloblastoma, identified 431 of 15,495 human-mouse orthologs that were upregulated in human mut*DDX3X* vs. wt*DDX3X* WNT-medulloblastoma (Figure S5). Ten percent (42/431) of these genes were also upregulated in *mWnt;Ddx3x*$^{Flx/Y}$ tumors (overlap representation factor=1.4, p=0.01) and were enriched for regulators of the cell stress (FDR=0.04 to 0.009) and immune response (FDR=0.03 to 1.2e^{-4}), including: *CCL2, SPINT1, SERTAD4, IFIT3, IFI44L, LRRC15, GCH1, DUSP9, RSAD2*, and *SELL* implicated in inflammasome and innate immune signaling (Khan et al., 2015; Kitajima et al., 2018; Mathias et al., 2007; McNeill et al., 2018; O'Prey et al., 2008; Unamuno et al., 2019); and *TRPV4* and *NEXN* that are implicated in neural inflammation (Khsheibun et al., 2014; Ye et al., 2012). Together, these data support the notion that *DDX3X* mediates a tumor suppressing, stress/inflammasome response in both human and mouse WNT-medulloblastoma that is partially relieved by loss of gene function.

DISCUSSION

DDX3X regulates an array of cell processes ranging from gene transcription and translation to the stress response (Herdy et al., 2018; Oh et al., 2016; Samir et al., 2019; Soto-Rifo et al., 2012; Valentin-Vega et al., 2016). Medulloblastoma-associated mutations in *DDX3X* have been shown to sequester DDX3X in stress granules and disrupt global patterns of gene translation (Oh et al., 2016; Valentin-Vega et al., 2016). But these studies have been conducted *in vitro*; therefore, it was unclear if *DDX3X* operates as a medulloblastoma oncogene or tumor suppressor gene. Here, we provide evidence that *DDX3X* serves as a key regulator of normal and malignant hindbrain development, suppressing WNT and SHH-medulloblastomas and restricting the competence of cell lineages to form these tumors.

Heterozygous, germline, missense mutations that disrupt *DDX3X* RNA helicase function account for up to 3% of intellectual disability in human females and cause hindbrain

developmental defects very similar to those that we observed in female *Blbp-Cre*$^{+/-}$*;Ddx3x*$^{Flx/Flx}$ mice (Dikow et al., 2017; Lennox et al., 2020; Nicola et al., 2019; Scala et al., 2019; Snijders Blok et al., 2015). Thus, *Ddx3x* deletion from the mouse brain phenocopies *DDX3X* loss-of-function mutations in humans. In our mice, aberrant hindbrain development was preceded by a highly-selective downregulation of *Hox* gene expression; suggesting strongly that Ddx3x patterns the hindbrain by regulating the transcription or stability of *Hox* RNAs. The transcription, splicing and stability of RNAs, including *Hox* transcripts, is critically dependent on guanine (G)-rich secondary structures in RNA termed G-quadruplexes (rG4) of which DDX3X is a key component (Herdy et al., 2018; Kwok et al., 2018; Kwok et al., 2016; Millevoi et al., 2012). Disruption of normal rG4s has been implicated in the pathogenesis of neurodegenerative diseases (Fay et al., 2017). Therefore, DDX3X might regulate *Hox* expression by maintaining transcript-associated rG4s. G4s also form within chromatin regulatory regions of DNA (dG4s) to control the transcription of *Hox* and other genes, and disruption of these structures has been implicated in cancer and neurodegeneration (Hansel-Hertsch et al., 2016; Lago et al., 2017; Zhang et al., 2018); therefore DDX3X might also regulate *Hox*-associated dG4s. Since *Hox* expression and brain development was largely unaffected in male *Blbp-Cre*$^{+/-}$*;Ddx3x*$^{Flx/Y}$ mice, we propose that the paralog *Ddx3y* substitutes for Ddx3x during neurodevelopment, perhaps by substituting in rG4 and dG4s. This notion is consistent with the rarity of intellectual problems in human males with germline mutations in *DDX3X* and evidence that *Ddx3y* regulates NPC differentiation *in vitro* (Vakilian et al., 2015).

Our finding that *Blbp-Cre*$^{+/-}$*;Ddx3x*$^{Flx/Flx}$ hindbrains also dysregulate cell stress, death and immune responses, unmasks a second potential function of *DDX3X* in normal and malignant hindbrain development –regulation of stress granule-inflammasome signaling. Ddx3x is a critical component of stress granules and inflammasomes (Samir et al., 2019; Shih et al., 2012). These multi-protein heteromeric complexes orchestrate the cell stress response and have been implicated in the pathogenesis of neurodegeneration and cancer (Anderson et al., 2015; Gan et al., 2018; Ivanov et al., 2019; Karki and Kanneganti, 2019; McKenzie et al., 2019a; Protter and Parker, 2016; Samir et al., 2019; Voet et al., 2019). Recently, we showed that Ddx3x shuttles between stress granules and inflammasomes to regulate cell fate choice in response to stress (Samir et al., 2019): incorporation of Ddx3x into stress granules promotes a cell survival signal, while its inclusion in inflammasomes drives pyroptosis - a form of programmed cell death important in the innate immune response and neurodegeneration (McKenzie et al., 2019a; Voet et al., 2019). Cre-recombination of *Ddx3x*$^{Flx/Flx}$ prevents Ddx3x incorporation in inflammasomes, blocking pyroptotic cell death signals and driving a default survival signal (Samir et al., 2019). Thus, disordered *Blbp-Cre*$^{+/-}$*;Ddx3x*$^{Flx/Flx}$ hindbrain development might be exacerbated postnatally by the failure of pyroptotic cell death to remove abnormal cells. Although *Ddx3y* does not restore the pyroptotic response in *Ddx3x*$^{Flx/Y}$ recombined cells (Samir et al., 2019), *Blbp-Cre*$^{+/-}$*;Ddx3x*$^{Flx/Y}$ hindbrains developed relatively normally and did not display aberrant cell stress, immune or death responses. Thus, analogous to the triggering of stress granule-inflammasome responses by amyloid-beta plaques in the brains of patients with Alzheimer's disease (McKenzie et al., 2019a), abnormal hindbrain patterning in *Blbp-Cre*

$^{+/-}$;*Ddx3x*$^{Flx/Flx}$ mice - a feature absent from *Blbp-Cre*$^{+/-}$;*Ddx3x*$^{Flx/Y}$ hindbrains - might trigger stress signals to which these mice are unable to respond appropriately (Figure 7).

Our data also provide strong evidence that *DDX3X* functions as a medulloblastoma tumor suppressor gene: a notion compatible with studies of >4,100 cancers, including medulloblastoma, that identified *DDX3X* as an 'escape from X-inactivation tumor-suppressor' or EXIST gene (Dunford et al., 2017). Thus, male medulloblastomas harboring missense mutations that inactivate gene function do not require deletion of a second allele (Lennox et al., 2020). In female medulloblastoma, *DDX3X* might function as a haploinsufficient tumor suppressor gene or the remaining wild-type allele could undergo X-inactivation since this process is variable and context dependent (Garieri et al., 2018).

Particularly remarkable was our observation that deletion of *Ddx3x* increased the penetrance of both mWnt and mShh-medulloblastomas and derestricted the cell lineages able to form these tumors. We therefore provide an explanation for the frequent mutation of *DDX3X* in both of these tumor subtypes in humans, and insight into the mechanism(s) that establish medulloblastoma subtypes. Specifically, our RNAseq and immunohistochemical studies of premalignant cerebella showed that aberrant Wnt signaling in cerebellar granule NPCs provokes a potent oncogenic-stress response that was removed partially by the deletion of *Ddx3x*. Aberrant Wnt-, rather than Shh-signalling, provoked this profound stress response in cerebellar granule NPCs likely because the latter and not the former is a primary mitogen for this cell lineage. Therefore, we propose that *DDX3X* functions as a medulloblastoma tumor suppressor by activating inflammasome-mediated pyroptotic cell death in response to oncogenic stress (Figure 7). In doing so, *DDX3X* serves as a gatekeeper of WNT and SHH-medulloblastoma subtypes, removing SHH-mutant lower rhombic lip and WNT-mutant granule NPCs, contributing to the exquisite restriction of oncogenic WNT and SHH pathway mutations to these tumor types in upper and lower rhombic lip derived medulloblastomas, respectively. We are performing additional studies of *Ddx3x* suppression of *mShh;Ddx3x*$^{Flx/Y}$ and *mShh;Ddx3x*$^{Flx/Flx}$ brainstem tumorigenesis since limited tumor material precluded an equally thorough assessment of the origin of these tumors.

An important question raised by our work, is the extent to which *DDX3X* suppresses lineage origins of WNT and SHH-medulloblastomas in humans. In other words, what proportion of WNT and SHH-medulloblastomas, if any, arise from granule and lower rhombic lip NPCs, respectively, and do these harbor mutations in *DDX3X*? Answering this question will require meticulous correlation between pre-operative tumor imaging, inter-operative observation and tumor transcriptome and mutational landscape mapping. But existing imaging data suggest a proportion of WNT and SHH-medulloblastomas might arise from cerebellar granule and lower rhombic lip mossy fiber NPCs, respectively. The great majority of WNT-medulloblastomas are located in and around the cerebellar pontine angle and infiltrate the brainstem (Patay et al., 2015; Perreault et al., 2014); however, around 10% of cases do not involve the brainstem, with rare WNT-medulloblastomas being confined solely to the cerebellum (Di Giannatale et al., 2016). Similarly, while the majority of SHH-medulloblastomas are lateralized within the cerebellar hemispheres, a small proportion are found outside of the cerebellum, with rare cases being confined to the brainstem (Demir et al., 2019). It is noteworthy that patient age, tumor location and *DDX3X* mutational status are

tightly correlated among human SHH-medulloblastomas: only 2% of SHH-medulloblastomas arising in patients aged ≤18 years mutate *DDX3X* and the majority are found in the cerebellar midline; conversely, 52% of adult SHH-medulloblastomas mutate *DDX3X* and almost all these tumors are located within the cerebellar hemispheres. Thus, adult SHH-medulloblastoma might arise within a distinct neural lineage in which *DDX3X* is particularly proficient at suppressing oncogenic signals.

It is important to note that while our mouse models delete Ddx3x, human medulloblastomas contain mainly heterozygous missense mutations in the gene (Northcott et al., 2019). However, evidence suggests that these alterations are likely to be functionally equivalent: developmental defects in *Blbp-Cre*$^{+/-}$*;Ddx3x*$^{Flx/Flx}$ mice are strikingly similar to those seen in humans with *de novo*, heterozygous, germline *DDX3X* mutations; several missense mutations observed in humans with developmental defects are identical to those observed in medulloblastoma; and these mutations have been shown to impair RNA helicase activity and be functionally equivalent to knock-out of *Ddx3x* in the developing forebrain (Dikow et al., 2017; Lennox et al., 2020; Nicola et al., 2019; Scala et al., 2019; Snijders Blok et al., 2015). Furthermore, a common feature of *DDX3X* mutations associated with both developmental defects and medulloblastoma, is their capacity to sequester DDX3X within stress granules: the greater the degree of sequestration, the more severe the phenotype (Lennox et al., 2020; Valentin-Vega et al., 2016). Diversion of DDX3X into stress granules and away from inflammasomes would block pyroptotic cell death, resulting in a default cell survival signal and persistence of *DDX3X*-mutant tumor cells (Figure 7).

Finally, the discovery that DDX3X signaling suppresses both WNT and SHH-medulloblastomas opens up potential new avenues to treat these tumors. Extensive drug discovery programs yielding both DDX3X agonists and antagonists have been stimulated by evidence that DDX3X is a component of critical host-cell pathways, hijacked by several pathogenic human viruses (Brai et al., 2019; Valiente-Echeverría et al., 2015). We are currently working with groups studying infectious diseases to determine if DDX3X agonists might be used to restore gene function and pyroptotic response in medulloblastomas in which the gene is mutated.

STAR METHODS

RESOURCE AVAILABILITY

Lead Contact—Further information and requests for resources and reagents should be directed to and will be fulfilled by the Lead Contact, Richard Gilbertson (Richard.gilbertson@cruk.cam.ac.uk).

Materials Availability—The *Ddx3x*^{Flx} mouse line used in this study was generated by the authors and described previously. The line is available freely from the author and is in the process of being deposited with Jax. Mouse medulloblastoma cells generated from mice that are described in this study are available freely from the lead contact under a standard Materials Transfer Agreement. Only costs to cover post and packaging will be requested.

Data and Code Availability—The RNA and DNA sequencing datasets generated during this study have been submitted to the GEO database (Accession ID: GSE147178 for RNA-sequencing and GSE147069 for DNA-sequencing). Other RNA sequencing sets that were previously published are referenced and available as indicated in the respective papers.

EXPERIMENTAL MODEL AND SUBJECT DETAILS

Genetically Engineered Models—All animal studies were performed under the Animals (Scientific Procedures) Act 1986 in accordance with UK Home Office licenses (Project License 70–8798, P6787677F) and approved by the Cancer Research UK (CRUK) Cambridge Institute Animal Welfare and Ethical Review Board. Mice were maintained in conventional cages and given access to standard diet and water. The developmental stage, sex and number of animals in each experiment is reported directly in the main Results section of the manuscript. Since our studies focused on the X-linked gene *Ddx3x*, then mice were not randomly assigned by sex to study groups. Control groups included an equal number of relevant sex animals unless indicated.

Generation of the *Ddx3x* conditional allele ($Ddx3x^{Flx}$) was detailed previously (Samir et al., 2019). Briefly, the *Ddx3x* allele was modified using CRISPR-Cas9 gene editing. Pronuclear stage zygotes were injected with two single guide RNAs targeting intron 6 and 14 of *Ddx3x*, Cas9 mRNA transcripts and homology directed repair oligonucleotides (*Ddx3x*-Intron6-LoxP-HDR and *Ddx3x*-Intron14-LoxP-HDR) designed to incorporate loxP sites together with EcoRI restriction sites to facilitate targeting and genotyping. Mice carrying the $Ddx3x^{Flx}$ allele were then bred with those harbouring the *Blbp-Cre* allele resulting in deletion of exons to 7–14 of the recombined $Ddx3x^{Flx}$ allele. *mWnt* mice were described previously (Gibson et. al., 2010). *mShh*medulloblastomas were generated by breeding mice carrying the $Blbp\text{-}Cre^{+/-}$ allele with B6N.129-Ptch1^{tm1Hahn}/J mice (The Jackson Laboratory, 012457).

Orthotopic allografting of mouse tumors—Mouse tumors were allografted into 4–6 week old female CD1-Foxn1^{NU} mice (Charles River, 086) exactly as described previously (Mohankumar et al., 2015). Briefly, 5×10^5 cells transduced with a YFP-luciferase lentivirus were re-suspended in 5μl matrigel (Corning, 354230) and injected via the cistern magna into the cerebellum of anaesthetised CD1-Foxn1^{NU} mice. Mice were monitored daily for neurological symptoms and weekly using bioluminescence imaging to detect tumor growth.

METHOD DETAILS

Western Blot Analysis—Cell pellets were harvested and lysed using RIPA lysis buffer (Invitrogen, 89901). 20μg of protein derived from relevant cell pellets were loaded into each lane of a standard SDS-PAGE gel and resolved by electrophoresis (Thermo Fisher Scientific, NP0335). Following transfer to 0.2μm nitrocellulose membrane (Thermo Fisher Scientific, IB301001), membranes were exposed to primary antibodies directed against Ddx3x (Bethyl, A300–474A) and beta-actin (Cell Signaling, 4967) and 1:15,000 dilution of anti-rabbit IRDye680LT-conjugated secondary antibody (LI-COR, 926–68023). Antibody binding to proteins was detected using the LI-COR Odyssey CLx.

Histology and Analysis—Tissue samples were formalin fixed, paraffin embedded and cut into 5μm sections as described (Gibson et al., 2010). Hematoxylin and Eosin (H&E) staining (Thermo Fisher Scientific, 7221 and 7111), was performed according to manufacturer's instructions. For the nissl staining, sections were stained with 0.5% cresyl fast violet (Sigma-Aldrich, H3757) for 10 minutes, washed with ultra-pure water followed by 0.25% acetic acid (Sigma-Aldrich, A6283) to clear the background stain. Sections were then dehydrated through serial alcohol solutions, rinsed in xylene and cover slipped. Immunohistochemistry was performed using the Leica Polymer Refine Detection System (Leica Biosystems, DS9800) together with the automated Bond platform. Primary antibodies included: Ki67 (1:1000; Bethyl, IHC-00375), cleaved caspase 3 (1:200; Cell Signaling, 9664), p21 (1:100; BD Biosciences, 556431), CD3 (Agilent Dako, A0452), CD45 (Abcam, ab25386), CD68 (Abcam, ab53444) and F4/80 (Bio-Rad, MCA497). Secondary (post primary) antibodies were anti-rabbit Poly-HRP-IgG (included in kit) and rabbit anti-mouse IgG1 (1:1500; Abcam, ab6728). Sections were then dehydrated through serial alcohol solutions, rinsed in xylene and cover slipped. Digital images of entire tissue sections were generated using the Leica Aperio AT2 digital scanner. Images were captured at 20x magnification, with a resolution of 0.5uM/pixel. Images were then viewed using the Leica Aperio Image Scope v12.3.2.8013 and staining quantified automatically using the Aperio ePathology image analysis software.

Immunofluorescence Staining—Immunofluorescence was performed using sections of formalin fixed, paraffin embedded tissue generated as described above. Antigen retrieval in tissue sections was achieved using pressure-cooking in citrate buffer pH6 for 20 minutes. Tissue sections were incubated with primary antibodies for 1 hour at room temperature.

Primary antibodies included: Ki67 (1:200; Abcam, ab15580 and 1:500; Thermo Fisher Scientific, 14-5698-82), Calbindin (1:50; Millipore, AB1778), Contactin2 (1:75; R&D Systems, AF4439), Lef1 (1:500; Abcam, ab137872), Pax6 (1:200; Biolegend, 901301), G3BP1 (1:100; Proteintech, 66486-1-Ig), Gfap (1:500; Dako, Z0334), NeuN (1:200; Millipore, MAB377), Irf1 (1:100; Abcam, ab240299), Iba1 (1:500; Wako, 013-27691) and Synaptophysin (1:100; Cell Signaling, 9020). Following washing, tissue sections where then incubated for 1 hour at room temperature in secondary antibody. Secondary antibodies included Alexa 488, 594 or 680 (1:200; Invitrogen, A-21206, A-21207 or A10043). Sections were then counterstained using DAPI (Cell Signaling, 4083) and mounted using ProLong Gold antifade mountant (Thermo Fisher Scientific, P36930). Digital images of tissue sections were captured using a Zeiss ImagerM2 and Apotome microscope.

In Situ Hybridisation—*Ddx3x* RNA expression was detected in formalin fixed paraffin embedded tissue sections simultaneously with mouse Gbx2, Otx2, Pax5, Atoh1 or Hoxa2 (see probe details in STAR Methods Table) using the Advanced Cell Diagnostics (ACD) RNAscope® 2.5 LS Duplex Reagent Kit (ACD, 322440). Briefly, 5μM thick, freshly cut sections were baked for 1 hour at 60°C and then loaded onto a Bond RX instrument (Leica Biosystems). Slides were deparaffinized and rehydrated on board the Bond RX before pre-treatment with Epitope Retrieval Solution 2 (Leica Biosystems, AR9640,) at 95°C for 10 minutes, and ACD Enzyme (Duplex Reagent kit) at 40°C for 15 minutes. Probe

hybridisation and signal amplification was performed according to manufacturer's instructions. Fast red detection of mouse Gbx2, Otx2, Pax5, Atoh1, or Hoxa2 was performed on the Bond Rx using the Bond Polymer Refine Red Detection Kit (Leica Biosystems, DS9390) according to manufacturer's protocol. Slides were then removed from the Bond Rx and detection of *Ddx3x* RNA performed using the RNAscope® 2.5 LS Green Accessory Pack (ACD, 322550) according to kit instructions. Slides were heated at 60°C for 1 hour, dipped in xylene and mounted using VectaMount permanent mounting medium (Vector Laboratories, H-5000). The slides were imaged on the Aperio AT2 (Leica Biosystems) to create whole slide images. Images were captured at 40x magnification, with a resolution of 0.25 microns per pixel.

RNA and DNA Extractions—Total RNA was extracted from tissue material using the RNeasy Plus universal kit (Qiagen, 73404) and stored at −80° C. DNA was extracted from 30μm thick formalin fixed, paraffin tissue sections using the truXTRAC FFPE total NA Plus Kit (Covaris, 520255) followed by magnetic bead-based DNA purification. DNA quality was verified using Tapestation (Agilent).

Library Preparation and Sequencing—All library preparation and sequencing were performed by the Genomics Core at the CRUK Cambridge Institute. The Illumina TruSeq stranded mRNA kit (Illumina, 20020595) was used to prepare RNA libraries and RNA quality confirmed using Tapestation (Agilent) and quantified using Kapa qPCR library quantification kit for Illumina platforms (Kapa Biosystems, KK4873). Samples were normalised using the Agilent Bravo, pooled and sequenced on Illumina HiSeq 4000 to generate single end 50bp reads at 20M reads per sample. DNA sequencing was performed on DNA libraries prepared using Nextera Flex preenrichment kit (Illumina) and sequenced on a NovaSeq SP flowcell generating paired end 50 reads at 20–42M reads per sample.

QUANTIFICATION AND STATISTICAL ANALYSIS

Quantitative histological analysis—Nuclear immunoreactivity for tested antigens was quantified using the nuclear v9 macro/algorithm (H&E, Ki67 and p21) and cytoplasmic immunoreactivity using the cytoplasmic v2 macro/algorithm (cleaved caspase 3). The identical pipeline was used for all tissue sections. The percentage of positive cells in each tissue section identified using these algorithms was recorded relative to the total number of nuclei in each section. Details of the numbers of tissues employed in each analysis are reported directly in the relevant part of the text of the main Results section.

Analysis of RNA sequence data—Single end 50bp RNA reads were aligned to GRCm38 with HISAT2 (with default parameters), each individual BAM file sorted and annotated. Each sample was sequenced across several lanes; per-lane BAM files were merged into per-sample BAMs. Quality control metrics were collected for each file, including duplication statistics and number of reads assigned to genes. Reads were counted on annotated features with sub-reads featureCounts, providing 'total', 'aligned to the genome', and 'assigned to a gene' (i.e. included in the analysis) counts. Percentages of aligned bases were computed for several categories: coding, UTR, intronic, intergenic. Other quality control metrics were the percentage of reads on the correct strand, median coefficient

of variation of coverage, median 5' bias, median 3' bias, and the ratio of 5' to 3' coverage. Quality control also included an expression heatmap drawn using log2 transformed counts. Log2 transformed counts were generated from normalized counts using the *log2* function in R and *counts* function from DEseq2. Genes were regarded as displaying differential expression between sample cohorts if they displayed of ≥1 or ≤−1 log-fold differences in expression levels and an absolute difference in mean gene expression level between groups of >50. Differential Principal Component Analysis was carried out on variance-stabilizing-transformed raw counts using the 'vst' function from DESeq2. Details of the numbers of tissues employed in each analysis are reported directly in the relevant part of the text of the main Results section.

Normalised TPM counts of WNT-medulloblastoma single cell RNA sequencing were log-transformed and then passed into a Seurat object. Cells were filtered based on a minimum of 200 and maximum of 9000 genes per cell. Normalized counts were then passed directly to the *FindVariableFeatures* and *ScaleData* functions from the Seurat package. Effects from total counts of RNA were regressed out in the *ScaleData* function. Downstream clustering analysis was then carried out in the Seurat package using default parameters. Details of the numbers of tissues employed in each analysis are reported directly in the relevant part of the text of the main Results section.

Pathway analysis—Genes identified as up- or downregulated within bulk and single cell RNAseq profiles between different tissue and cell types were analyzed using g:GOST within the g:Profiler interface (Raudvere et al., 2019). g:GOST enabled identification of statistically enriched genes that over-representated Gene Ontology terms, biological pathways, regulatory DNA elements, human disease gene annotations, and protein-protein interaction networks. Visualization of patterns of pathway enrichment in g:GOST outputs were generated using Enrichment map within Cytoscape (Shannon et al., 2003).

DNA copy number analysis—Raw DNA sequence reads were aligned to the mm10 assembly of the mouse genome (mm10, Genome Reference Consortium Mouse Build 38 (GCA_000001635.2)) from UCSC. Read mapping was performed using the Burrows-Wheeler Aligner. Copy number variation analysis was performed in R (version 3.5.2) using the QDNAseq package (version 1.12.0) from Bioconductor. A bin size of 100kb was used for 'windowing' copy number. Segmentation of copy number was carried out using the DNAcopy package (version 1.56.0) and gains and losses were called using the CGHcall package (version 2.44.0).

Statistical tests and survival analysis—Survival analyses among animal cohorts of the genotype, number and sex defined in the main text was performed using the Log-Rank Mantel-Cox statistic. Statistical differences in tissue histology patterns e.g., number of immune-positive nuclei, among animal cohorts of the genotype, number and sex defined in the main text was performed using the non-parametric Mann-Whitney test. Details of the numbers of tissues employed in each analysis are reported directly in the relevant part of the text of the main Results section.

Supplementary Material

Refer to Web version on PubMed Central for supplementary material.

ACKNOWLEDGEMENTS

This work was supported by grants from the National Institutes of Health (R.J.G., P01CA96832, R01CA129541 and P30CA021765), the American Lebanese Syrian Associated Charities and Cancer Research UK. We are grateful to the staff of the BRU, Histology, Genomics, Bioinformatics, and Light Microscopy Core Facilities at the CRUK Cambridge Institute for technical assistance.

REFENCENCES

Anderson P, Kedersha N, and Ivanov P (2015). Stress granules, P-bodies and cancer. Biochim Biophys Acta 1849, 861–870. [PubMed: 25482014]

Brai A, Martelli F, Riva V, Garbelli A, Fazi R, Zamperini C, Pollutri A, Falsitta L, Ronzini S, Maccari L, et al. (2019). DDX3X Helicase Inhibitors as a New Strategy To Fight the West Nile Virus Infection. J Med Chem 62, 2333–2347. [PubMed: 30721061]

Dai H, Goto Y-I, and Itoh M (2017). Insulin-Like Growth Factor Binding Protein-3 Deficiency Leads to Behavior Impairment with Monoaminergic and Synaptic Dysfunction. Am J Pathol 187, 390–400. [PubMed: 28088287]

Demir MK, Yapıcıer Ö, Mert B, Alshareefi W, and Bozbuğa M (2019). Primary Sonic Hedgehog-activated dorsal brainstem medulloblastoma and ipsilateral cerebellar atrophy in an adult. Neuroradiol J, 1971400919892824–1971400919892824.

Di Giannatale A, Carai A, Cacchione A, Marrazzo A, Dell'Anna VA, Colafati GS, Diomedi-Camassei F, Miele E, Po A, Ferretti E, et al. (2016). Anomalous vascularization in a Wnt medulloblastoma: a case report. BMC Neurol 16, 103–103. [PubMed: 27416922]

Dikow N, Granzow M, Graul-Neumann LM, Karch S, Hinderhofer K, Paramasivam N, Behl L-J, Kaufmann L, Fischer C, Evers C, et al. (2017). DDX3X mutations in two girls with a phenotype overlapping Toriello-Carey syndrome. Am J Med Genet A 173, 1369–1373. [PubMed: 28371085]

Doherty GJ, Petruzzelli M, Beddowes E, Ahmad SS, Caldas C, and Gilbertson RJ (2019). Cancer Treatment in the Genomic Era. Annual Review of Biochemistry 88, 247–280.

Druker BJ, Talpaz M, Resta DJ, Peng B, Buchdunger E, Ford JM, Lydon NB, Kantarjian H, Capdeville R, Ohno-Jones S, and Sawyers CL (2001). Efficacy and safety of a specific inhibitor of the BCR-ABL tyrosine kinase in chronic myeloid leukemia. N Engl J Med 344, 1031–1037. [PubMed: 11287972]

Duijkers FA, McDonald A, Janssens GE, Lezzerini M, Jongejan A, van Koningsbruggen S, Leeuwenburgh-Pronk WG, Wlodarski MW, Moutton S, Tran-Mau-Them F, et al. (2019). HNRNPR Variants that Impair Homeobox Gene Expression Drive Developmental Disorders in Humans. Am J Hum Genet 104, 1040–1059. [PubMed: 31079900]

Dunford A, Weinstock DM, Savova V, Schumacher SE, Cleary JP, Yoda A, Sullivan TJ, Hess JM, Gimelbrant AA, Beroukhim R, et al. (2017). Tumor-suppressor genes that escape from X-inactivation contribute to cancer sex bias. Nat Genet 49, 10–16. [PubMed: 27869828]

Fay MM, Anderson PJ, and Ivanov P (2017). ALS/FTD-Associated C9ORF72 Repeat RNA Promotes Phase Transitions In Vitro and in Cells. Cell Rep 21, 3573–3584. [PubMed: 29262335]

Forones NM, Lima FT, Martin RP, Martins L, Teixeira PVL, Pesquero JB, Oshima CTF, and Pimenta CAM (2018). Mismatch Repair Genes and EPCAM germline mutations in patients with gastric or colorectal cancer with suspected of Lynch syndrome. Journal of Clinical Oncology 36, e13623–e13623.

Gajjar A, Chintagumpala M, Ashley D, Kellie S, Kun LE, Merchant TE, Woo S, Wheeler G, Ahern V, Krasin MJ, et al. (2006). Risk-adapted craniospinal radiotherapy followed by high-dose chemotherapy and stem-cell rescue in children with newly diagnosed medulloblastoma (St Jude Medulloblastoma-96): long-term results from a prospective, multicentre trial. The Lancet Oncology 7, 813–820. [PubMed: 17012043]

Gan L, Cookson MR, Petrucelli L, and La Spada AR (2018). Converging pathways in neurodegeneration, from genetics to mechanisms. Nat Neurosci 21, 1300–1309. [PubMed: 30258237]

Garieri M, Stamoulis G, Blanc X, Falconnet E, Ribaux P, Borel C, Santoni F, and Antonarakis SE (2018). Extensive cellular heterogeneity of X inactivation revealed by single-cell allele-specific expression in human fibroblasts. Proceedings of the National Academy of Sciences 115, 13015–13020.

Gibson P, Tong Y, Robinson G, Thompson MC, Currle DS, Eden C, Kranenburg TA, Hogg T, Poppleton H, Martin J, et al. (2010). Subtypes of medulloblastoma have distinct developmental origins. Nature 468, 1095–1099. [PubMed: 21150899]

Hansel-Hertsch R, Beraldi D, Lensing SV, Marsico G, Zyner K, Parry A, Di Antonio M, Pike J, Kimura H, Narita M, et al. (2016). G-quadruplex structures mark human regulatory chromatin. Nat Genet 48, 1267–1272. [PubMed: 27618450]

Herdy B, Mayer C, Varshney D, Marsico G, Murat P, Taylor C, D'Santos C, Tannahill D, and Balasubramanian S (2018). Analysis of NRAS RNA G-quadruplex binding proteins reveals DDX3X as a novel interactor of cellular G-quadruplex containing transcripts. Nucleic Acids Res 46, 11592–11604. [PubMed: 30256975]

Hovestadt V, Smith KS, Bihannic L, Filbin MG, Shaw ML, Baumgartner A, DeWitt JC, Groves A, Mayr L, Weisman HR, et al. (2019). Resolving medulloblastoma cellular architecture by single-cell genomics. Nature 572, 74–79. [PubMed: 31341285]

Ivanov P, Kedersha N, and Anderson P (2019). Stress Granules and Processing Bodies in Translational Control. Cold Spring Harbor perspectives in biology 11, a032813. [PubMed: 30082464]

Jessa S, Blanchet-Cohen A, Krug B, Vladoiu M, Coutelier M, Faury D, Poreau B, De Jay N, Hébert S, Monlong J, et al. (2019). Stalled developmental programs at the root of pediatric brain tumors. Nat Genet 51, 1702–1713. [PubMed: 31768071]

Jones DTW, Jager N, Kool M, Zichner T, Hutter B, Sultan M, Cho Y-J, Pugh TJ, Hovestadt V, Stutz AM, et al. (2012). Dissecting the genomic complexity underlying medulloblastoma. Nature 488, 100–105. [PubMed: 22832583]

Karki R, and Kanneganti T-D (2019). Diverging inflammasome signals in tumorigenesis and potential targeting. Nature reviews Cancer 19, 197–214. [PubMed: 30842595]

Kawauchi D, Robinson G, Uziel T, Gibson P, Rehg J, Gao C, Finkelstein D, Qu C, Pounds S, Ellison David W., et al. (2012). A Mouse Model of the Most Aggressive Subgroup of Human Medulloblastoma. Cancer Cell 21, 168–180. [PubMed: 22340591]

Khan KA, Dô F, Marineau A, Doyon P, Clément J-F, Woodgett JR, Doble BW, and Servant MJ (2015). Fine-Tuning of the RIG-I-Like Receptor/Interferon Regulatory Factor 3-Dependent Antiviral Innate Immune Response by the Glycogen Synthase Kinase 3/β-Catenin Pathway. Mol Cell Biol 35, 3029–3043. [PubMed: 26100021]

Khsheibun R, Paperna T, Volkowich A, Lejbkowicz I, Avidan N, and Miller A (2014). Gene expression profiling of the response to interferon beta in Epstein-Barr-transformed and primary B cells of patients with multiple sclerosis. PLoS One 9, e102331–e102331. [PubMed: 25025430]

Kiecker C, and Lumsden A (2005). Compartments and their boundaries in vertebrate brain development. Nat Rev Neurosci 6, 553–564. [PubMed: 15959467]

Kitajima S, Asahina H, Chen T, Guo S, Quiceno LG, Cavanaugh JD, Merlino AA, Tange S, Terai H, Kim JW, et al. (2018). Overcoming Resistance to Dual Innate Immune and MEK Inhibition Downstream of KRAS. Cancer Cell 34, 439–452.e436. [PubMed: 30205046]

Kwok CK, Marsico G, and Balasubramanian S (2018). Detecting RNA G-Quadruplexes (rG4s) in the Transcriptome. Cold Spring Harbor Perspectives in Biology 10.

Kwok CK, Marsico G, Sahakyan AB, Chambers VS, and Balasubramanian S (2016). rG4-seq reveals widespread formation of G-quadruplex structures in the human transcriptome. Nat Methods 13, 841–844. [PubMed: 27571552]

Lago S, Tosoni E, Nadai M, Palumbo M, and Richter SN (2017). The cellular protein nucleolin preferentially binds long-looped G-quadruplex nucleic acids. Biochim Biophys Acta Gen Subj 1861, 1371–1381. [PubMed: 27913192]

Lennox AL, Hoye ML, Jiang R, Johnson-Kerner BL, Suit LA, Venkataramanan S, Sheehan CJ, Alsina FC, Fregeau B, Aldinger KA, et al. (2020). Pathogenic DDX3X Mutations Impair RNA Metabolism and Neurogenesis during Fetal Cortical Development. Neuron.

Letai A (2017). Functional precision cancer medicine—moving beyond pure genomics. Nature Medicine 23, 1028–1035.

Li H, and Durbin R (2010). Fast and accurate long-read alignment with Burrows-Wheeler transform. Bioinformatics (Oxford, England) 26, 589–595.

Liao Y-C, Fernandopulle MS, Wang G, Choi H, Hao L, Drerup CM, Patel R, Qamar S, Nixon-Abell J, Shen Y, et al. (2019). RNA Granules Hitchhike on Lysosomes for Long-Distance Transport, Using Annexin A11 as a Molecular Tether. Cell 179, 147–164.e120. [PubMed: 31539493]

Love MI, Huber W, and Anders S (2014). Moderated estimation of fold change and dispersion for RNA-seq data with DESeq2. Genome biology 15, 550. [PubMed: 25516281]

Makki N, and Capecchi MR (2011). Identification of novel Hoxa1 downstream targets regulating hindbrain, neural crest and inner ear development. Dev Biol 357, 295–304. [PubMed: 21784065]

Mathias JR, Dodd ME, Walters KB, Rhodes J, Kanki JP, Look AT, and Huttenlocher A (2007). Live imaging of chronic inflammation caused by mutation of zebrafish Hai1. J Cell Sci 120, 3372–3383. [PubMed: 17881499]

McKenzie BA, Dixit VM, and Power C (2019a). Fiery Cell Death: Pyroptosis in the Central Nervous System. Trends Neurosci, S0166–2236(0119)30218–30218.

McKenzie LD, LeClair JW, Miller KN, Strong AD, Chan HL, Oates EL, Ligon KL, Brennan CW, and Chheda MG (2019b). CHD4 regulates the DNA damage response and RAD51 expression in glioblastoma. Sci Rep 9, 4444–4444. [PubMed: 30872624]

McNeill E, Stylianou E, Crabtree MJ, Harrington-Kandt R, Kolb A-L, Diotallevi M, Hale AB, Bettencourt P, Tanner R, O'Shea MK, et al. (2018). Regulation of mycobacterial infection by macrophage Gch1 and tetrahydrobiopterin. Nature communications 9, 5409–5409.

Millevoi S, Moine H, and Vagner S (2012). G-quadruplexes in RNA biology. Wiley Interdiscip Rev RNA 3, 495–507. [PubMed: 22488917]

Mohankumar KM, Currle DS, White E, Boulos N, Dapper J, Eden C, Nimmervoll B, Thiruvenkatam R, Connelly M, Kranenburg TA, et al. (2015). An in vivo screen identifies ependymoma oncogenes and tumor-suppressor genes. Nat Genet 47, 878–887. [PubMed: 26075792]

Nicola P, Blackburn PR, Rasmussen KJ, Bertsch NL, Klee EW, Hasadsri L, Pichurin PN, Rankin J, Raymond FL, Study DDD, and Clayton-Smith J (2019). De novo DDX3X missense variants in males appear viable and contribute to syndromic intellectual disability. Am J Med Genet A 179, 570–578. [PubMed: 30734472]

Northcott PA, Jones DTW, Kool M, Robinson GW, Gilbertson RJ, Cho Y-J, Pomeroy SL, Korshunov A, Lichter P, Taylor MD, and Pfister SM (2012a). Medulloblastomics: the end of the beginning. Nat Rev Cancer 12, 818–834. [PubMed: 23175120]

Northcott PA, Korshunov A, Witt H, Hielscher T, Eberhart CG, Mack S, Bouffet E, Clifford SC, Hawkins CE, French P, et al. (2011). Medulloblastoma Comprises Four Distinct Molecular Variants. Journal of Clinical Oncology 29, 1408–1414. [PubMed: 20823417]

Northcott PA, Robinson GW, Kratz CP, Mabbott DJ, Pomeroy SL, Clifford SC, Rutkowski S, Ellison DW, Malkin D, Taylor MD, et al. (2019). Medulloblastoma. Nature Reviews Disease Primers 5, 11.

Northcott PA, Shih DJH, Peacock J, Garzia L, Sorana Morrissy A, Zichner T, Stutz AM, Korshunov A, Reimand J, Schumacher SE, et al. (2012b). Subgroup-specific structural variation across 1,000 medulloblastoma genomes. Nature 488, 49–56. [PubMed: 22832581]

O'Prey J, Wilkinson S, and Ryan KM (2008). Tumor antigen LRRC15 impedes adenoviral infection: implications for virus-based cancer therapy. J Virol 82, 5933–5939. [PubMed: 18385238]

Oh S, Flynn RA, Floor SN, Purzner J, Martin L, Do BT, Schubert S, Vaka D, Morrissy S, Li Y, et al. (2016). Medulloblastoma-associated DDX3 variant selectively alters the translational response to stress. Oncotarget 7, 28169–28182. [PubMed: 27058758]

Patay Z, DeSain LA, Hwang SN, Coan A, Li Y, and Ellison DW (2015). MR Imaging Characteristics of Wingless-Type-Subgroup Pediatric Medulloblastoma. AJNR Am J Neuroradiol 36, 2386–2393. [PubMed: 26338912]

Perreault S, Ramaswamy V, Achrol AS, Chao K, Liu TT, Shih D, Remke M, Schubert S, Bouffet E, Fisher PG, et al. (2014). MRI surrogates for molecular subgroups of medulloblastoma. AJNR Am J Neuroradiol 35, 1263–1269. [PubMed: 24831600]

Protter DSW, and Parker R (2016). Principles and Properties of Stress Granules. Trends Cell Biol 26, 668–679. [PubMed: 27289443]

Pugh TJ, Weeraratne SD, Archer TC, Pomeranz Krummel DA, Auclair D, Bochicchio J, Carneiro MO, Carter SL, Cibulskis K, Erlich RL, et al. (2012). Medulloblastoma exome sequencing uncovers subtype-specific somatic mutations. Nature 488, 106–110. [PubMed: 22820256]

Ratnaparkhe M, Wong JKL, Wei P-C, Hlevnjak M, Kolb T, Simovic M, Haag D, Paul Y, Devens F, Northcott P, et al. (2018). Defective DNA damage repair leads to frequent catastrophic genomic events in murine and human tumors. Nature Communications 9, 4760.

Raudvere U, Kolberg L, Kuzmin I, Arak T, Adler P, Peterson H, and Vilo J (2019). g:Profiler: a web server for functional enrichment analysis and conversions of gene lists (2019 update). Nucleic Acids Res 47, W191–W198. [PubMed: 31066453]

Robinson G, Parker M, Kranenburg TA, Lu C, Chen X, Ding L, Phoenix TN, Hedlund E, Wei L, Zhu X, et al. (2012). Novel mutations target distinct subgroups of medulloblastoma. Nature 488, 43–48. [PubMed: 22722829]

Roychowdhury S, and Chinnaiyan AM (2014). Translating Genomics for Precision Cancer Medicine. Annual Review of Genomics and Human Genetics 15, 395–415.

Samir P, Kesavardhana S, Patmore DM, Gingras S, Malireddi RKS, Karki R, Guy CS, Briard B, Place DE, Bhattacharya A, et al. (2019). DDX3X acts as a live-or-die checkpoint in stressed cells by regulating NLRP3 inflammasome. Nature 573, 590–594. [PubMed: 31511697]

Scala M, Torella A, Severino M, Morana G, Castello R, Accogli A, Verrico A, Vari MS, Cappuccio G, Pinelli M, et al. (2019). Three de novo DDX3X variants associated with distinctive brain developmental abnormalities and brain tumor in intellectually disabled females. Eur J Hum Genet 27, 1254–1259. [PubMed: 30936465]

Scheinin I, Sie D, Bengtsson H, van de Wiel MA, Olshen AB, van Thuijl HF, van Essen HF, Eijk PP, Rustenburg F, Meijer GA, et al. (2014). DNA copy number analysis of fresh and formalin-fixed specimens by shallow whole-genome sequencing with identification and exclusion of problematic regions in the genome assembly. Genome Res 24, 2022–2032. [PubMed: 25236618]

Shannon P, Markiel A, Ozier O, Baliga NS, Wang JT, Ramage D, Amin N, Schwikowski B, and Ideker T (2003). Cytoscape: a software environment for integrated models of biomolecular interaction networks. Genome Res 13, 2498–2504. [PubMed: 14597658]

Shih J-W, Wang W-T, Tsai T-Y, Kuo C-Y, Li H-K, and Wu Lee Y-H (2012). Critical roles of RNA helicase DDX3 and its interactions with eIF4E/PABP1 in stress granule assembly and stress response. Biochem J 441, 119–129. [PubMed: 21883093]

Snijders Blok L, Madsen E, Juusola J, Gilissen C, Baralle D, Reijnders MRF, Venselaar H, Helsmoortel C, Cho MT, Hoischen A, et al. (2015). Mutations in DDX3X Are a Common Cause of Unexplained Intellectual Disability with Gender-Specific Effects on Wnt Signaling. Am J Hum Genet 97, 343–352. [PubMed: 26235985]

Soto-Rifo R, Rubilar PS, Limousin T, de Breyne S, Décimo D, and Ohlmann T (2012). DEAD-box protein DDX3 associates with eIF4F to promote translation of selected mRNAs. EMBO J 31, 3745–3756. [PubMed: 22872150]

Tong Y, Merino D, Nimmervoll B, Gupta K, Wang Y-D, Finkelstein D, Dalton J, Ellison DW, Ma X, Zhang J, et al. (2015). Cross-Species Genomics Identifies TAF12, NFYC, and RAD54L as Choroid Plexus Carcinoma Oncogenes. Cancer Cell 27, 712–727. [PubMed: 25965574]

Tourrière H, Gallouzi IE, Chebli K, Capony JP, Mouaikel J, van der Geer P, and Tazi J (2001). RasGAP-associated endoribonuclease G3Bp: selective RNA degradation and phosphorylation-dependent localization. Mol Cell Biol 21, 7747–7760. [PubMed: 11604510]

Unamuno X, Gómez-Ambrosi J, Ramírez B, Rodríguez A, Becerril S, Valentí V, Moncada R, Silva C, Salvador J, Frühbeck G, and Catalán V (2019). NLRP3 inflammasome blockade reduces adipose tissue inflammation and extracellular matrix remodeling. Cell Mol Immunol, 10.1038/s41423-41019-40296-z.

Vakilian H, Mirzaei M, Sharifi Tabar M, Pooyan P, Habibi Rezaee L, Parker L, Haynes PA, Gourabi H, Baharvand H, and Salekdeh GH (2015). DDX3Y, a Male-Specific Region of Y Chromosome Gene, May Modulate Neuronal Differentiation. J Proteome Res 14, 3474–3483. [PubMed: 26144214]

Valentin-Vega YA, Wang Y-D, Parker M, Patmore DM, Kanagaraj A, Moore J, Rusch M, Finkelstein D, Ellison DW, Gilbertson RJ, et al. (2016). Cancer-associated DDX3X mutations drive stress granule assembly and impair global translation. Sci Rep 6, 25996–25996. [PubMed: 27180681]

Valiente-Echeverría F, Hermoso MA, and Soto-Rifo R (2015). RNA helicase DDX3: at the crossroad of viral replication and antiviral immunity. Rev Med Virol 25, 286–299. [PubMed: 26174373]

van de Wiel MA, Kim KI, Vosse SJ, van Wieringen WN, Wilting SM, and Ylstra B (2007). CGHcall: calling aberrations for array CGH tumor profiles. Bioinformatics (Oxford, England) 23, 892–894.

Vladoiu MC, El-Hamamy I, Donovan LK, Farooq H, Holgado BL, Sundaravadanam Y, Ramaswamy V, Hendrikse LD, Kumar S, Mack SC, et al. (2019). Childhood cerebellar tumours mirror conserved fetal transcriptional programs. Nature 572, 67–73. [PubMed: 31043743]

Voet S, Srinivasan S, Lamkanfi M, and van Loo G (2019). Inflammasomes in neuroinflammatory and neurodegenerative diseases. EMBO Mol Med 11, e10248. [PubMed: 31015277]

Weber A, Schwarz SC, Tost J, Trümbach D, Winter P, Busato F, Tacik P, Windhorst AC, Fagny M, Arzberger T, et al. (2018). Epigenome-wide DNA methylation profiling in Progressive Supranuclear Palsy reveals major changes at DLX1. Nature Communications 9, 2929.

Welstead GG, Creyghton MP, Bilodeau S, Cheng AW, Markoulaki S, Young RA, and Jaenisch R (2012). X-linked H3K27me3 demethylase Utx is required for embryonic development in a sex-specific manner. Proceedings of the National Academy of Sciences of the United States of America 109, 13004–13009. [PubMed: 22826230]

Wetmore C, Eberhart DE, and Curran T (2000). The Normal patched Allele Is Expressed in Medulloblastomas from Mice with Heterozygous Germ-Line Mutation of patched. Cancer Research 60, 2239–2246. [PubMed: 10786690]

Yang ZJ, Ellis T, Markant SL, Read TA, Kessler JD, Bourboulas M, Schuller U, Machold R, Fishell G, Rowitch DH, et al. (2008). Medulloblastoma can be initiated by deletion of Patched in lineage-restricted progenitors or stem cells. Cancer Cell 14, 135–145. [PubMed: 18691548]

Ye L, Kleiner S, Wu J, Sah R, Gupta RK, Banks AS, Cohen P, Khandekar MJ, Boström P, Mepani RJ, et al. (2012). TRPV4 is a regulator of adipose oxidative metabolism, inflammation, and energy homeostasis. Cell 151, 96–110. [PubMed: 23021218]

Zhang H, Xing L, Rossoll W, Wichterle H, Singer RH, and Bassell GJ (2006). Multiprotein complexes of the survival of motor neuron protein SMN with Gemins traffic to neuronal processes and growth cones of motor neurons. J Neurosci 26, 8622–8632. [PubMed: 16914688]

Zhang X, Zhao B, Yan T, Hao A, Gao Y, Li D, and Sui G (2018). G-quadruplex structures at the promoter of HOXC10 regulate its expression. Biochimica et biophysica acta Gene regulatory mechanisms 1861, 1018–1028. [PubMed: 30343692]

HIGHLIGHTS

- *DDX3X* is frequently mutated in the brain tumor medulloblastoma
- *Ddx3x* regulates hindbrain development via *Hox* gene expression and stress signaling
- *Ddx3x* supresses medulloblastoma by restricting tumor lineage origins

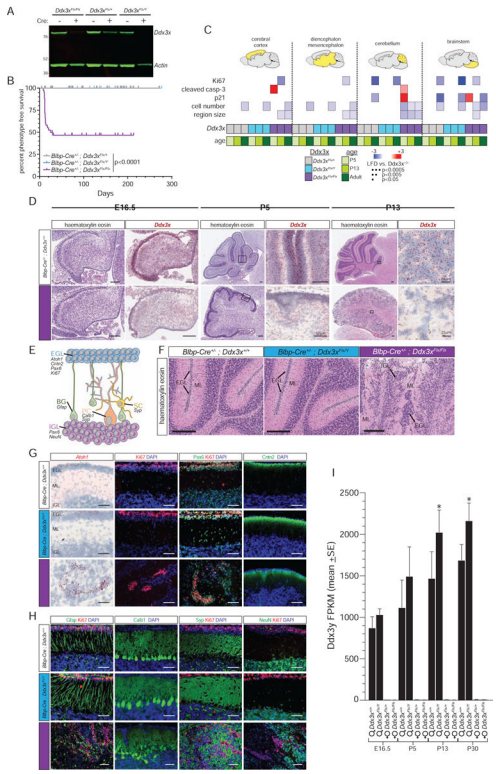

Figure 1. *Ddx3x* regulates hindbrain development.

A. Western blot of Ddx3x and actin loading control expression in Cre-recombined mouse NPCs of the indicated genotype. **B.** Phenotype-free survival of *Blbp-Cre*$^{+/-}$;*Ddx3x*$^{Flx/Flx}$ (n=55), *Blbp-Cre*$^{+/-}$;*Ddx3x*$^{Flx/+}$ (n=29) and *Blbp-Cre*$^{+/-}$;*Ddx3x*$^{Flx/Y}$ mice (n=31). **C.** Heatmaps reporting the log-fold difference in the indicated histological parameters quantified by automated photo-micromorphometry. Analyses were performed on ≥10 mice per time point for each indicated variable and genotype. **D.** Photomicrographs of morphology (hematoxylin and eosin stain) and Ddx3x RNA expression (*in situ* hybridization) in developing hindbrains of the indicated genotype (unless indicated scale bars=100μm). **E.** Microanatomy of the cerebellar cortex cells and associated markers used in F-H are: EGL=external germinal layer; IGL=internal granule cell layer; BG=Bergman glia; PC=Purkinje cell; SC=stellate cell. **F.** Photomicrographs of morphology (hematoxylin and eosin stain) of the P13 cerebellar cortex in the indicated mouse genotype (scale bars=100μm). **G, H.** *In situ* hybridization (Atoh1) and immunofluorescence of the indicated cell markers in P13 mouse cerebellar cortex of the indicated genotype. **I**. *Ddx3y* fragments per kilobase of transcript per million mapped reads in mouse hindbrain (n=3 to 5 per genotype, sex and age; *=p<0.05, Mann-Whitney). See also Figure S1.

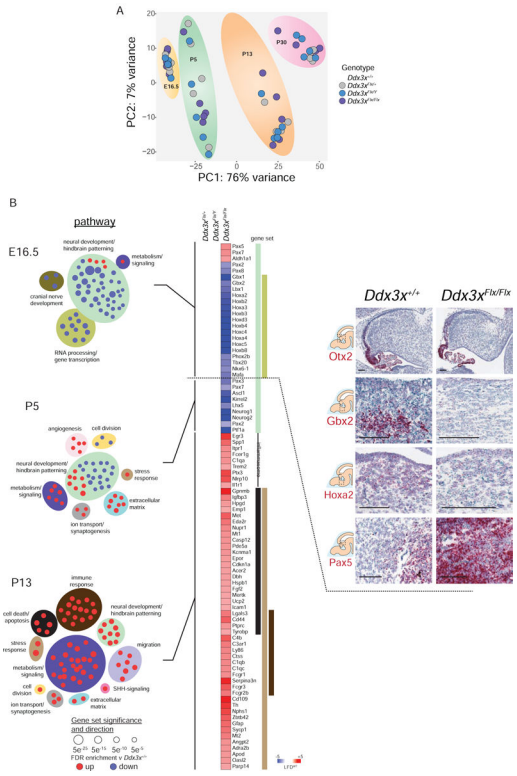

Figure 2. *Ddx3x* regulates tissue patterning and stress response in the hindbrain.

A. Principal components analysis of RNAseq profiles generated from hindbrains isolated from the indicated mice (≥5 hindbrains per timepoint and genotype). **B.** *Centre*, heat map of the log-fold difference of expression of the indicated genes in hindbrains of mice with the indicated genotypes relative to *Blbp-Cre*$^{+/-}$;*Ddx3x*$^{+/+}$ controls (≥5 hindbrains per timepoint and genotype at the indicated developmental time points). *Left*, Cytoscape™ plots identifying gene sets with related functions that are significantly up- or down-regulated in *Blbp-Cre*$^{+/-}$;*Ddx3x*$^{Flx/Flx}$ hindbrains relative to *Blbp-Cre*$^{+/-}$;*Ddx3x*$^{+/+}$ controls at the indicated developmental stage. *Right, in situ* hybridization of the indicated genes in *Blbp-Cre*$^{+/-}$;*Ddx3x*$^{Flx/Flx}$ and *Blbp-Cre*$^{+/-}$;*Ddx3x*$^{+/+}$ hindbrains. Cartoons indicate the location of the higher power images (scale bars=100μm). See also Figure S2.

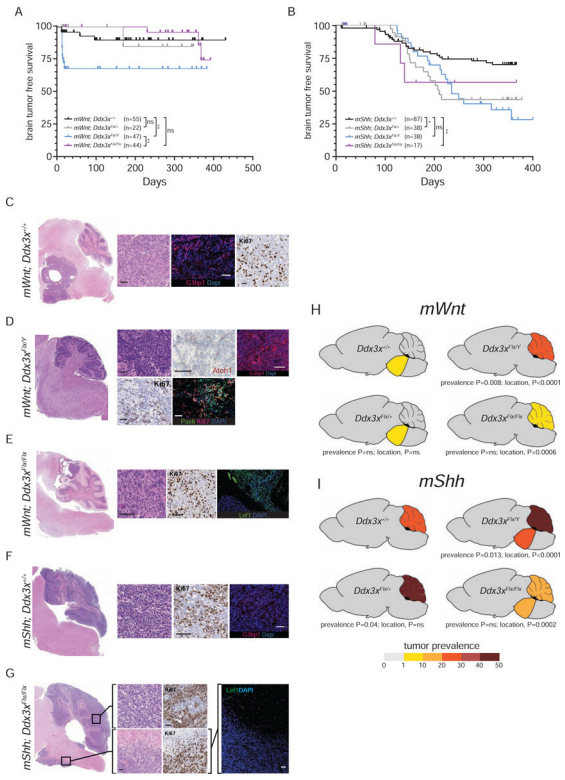

Figure 3. *Ddx3x* is a medulloblastoma tumor suppressor gene.

Tumor-free survival curves of mice predisposed to develop either Wnt- **(A)** or Shh-medulloblastoma **(B)** harboring the indicated *Ddx3x* alleles. Numbers of mice 'n' are shown for each cohort. ns=not significant, *=p<0.05, **=p<0.005, Log-Rank statistic. Photomicrographs of low and high-power images of tumors arising in mice predisposed to develop Wnt- **(C-E)** or Shh-medulloblastomas **(F,G)** harboring the indicated *Ddx3x* alleles. High power images reveal tumor morphology (hematoloxylin and eosin), proliferation (Ki67 immunohistochemical stain), or immunofluorescence of the indicated markers. T=tumor, (scale bars=100μm). Cartoons depicting the incidence and distribution (brainstem or cerebellum) of tumors arising in mice predisposed to develop either Wnt- **(H)** or Shh-medulloblastoma **(I)** harboring the indicated *Ddx3x* alleles. Mouse numbers same as in (A and B). See also Figure S3.

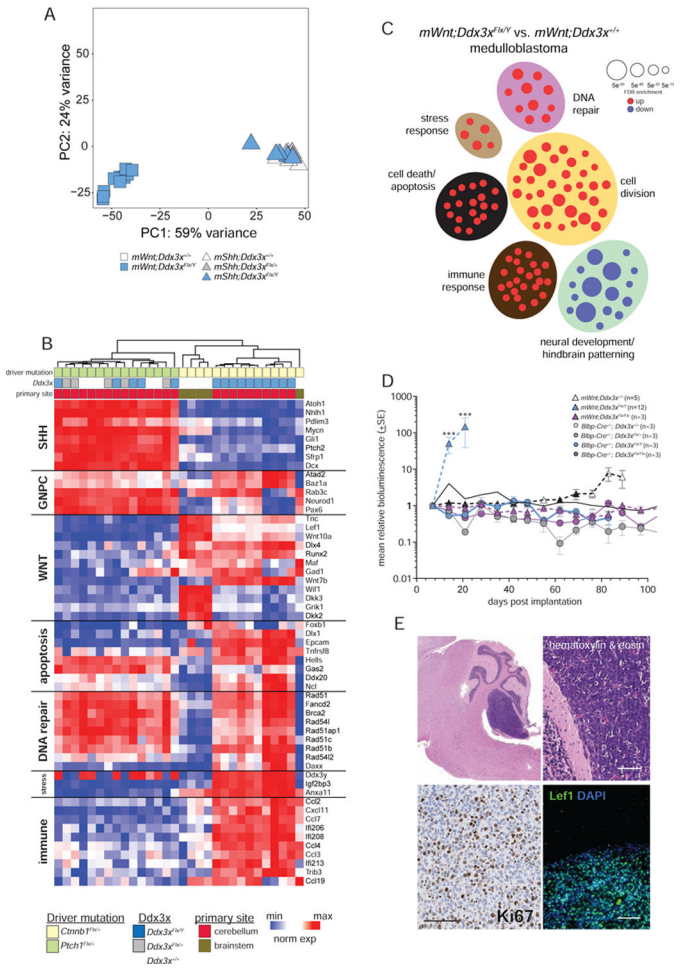

Figure 4. *Ddx3x* restricts cell lineage origins of Wnt-medulloblastoma.

A. Principal component analysis of RNAseq profiles generated from 30 mouse tumors (shown in B) arising in mice predisposed to develop Wnt- or Shh-medulloblastomas harboring the indicated *Ddx3x* alleles. **B.** Unsupervised hierarchical clustering of RNAseq profiles of 30 tumors shown in (A). Heatmap shows the log2 normalized expression values of the indicated genes. Gene set classification is shown left, including signature genes of WNT and SHH medulloblastoma. **C**. Cytoscape™ plot identifying gene sets with related functions that are significantly up- or down-regulated in *mWnt;Ddx3x*$^{Flx/Y}$ relative to *mWnt;Ddx3x*$^{+/+}$ tumors shown in A and B. **D.** Tumor growth recorded as bioluminescence in mice implanted with cells isolated from cerebella of the indicated genotype (number of mice implanted with each cell type is shown ‘n’; ***=p<0.0005, Mann-Whitney). **E.** Photomicrographs of tumor (T) arising in the cerebellum of a recipient mice implanted with cerebellar cells isolated from *mWnt;Ddx3x*$^{Flx/Y}$ mice. Images reveal tumor morphology (hematoloxylin and eosin), proliferation (Ki67 immunohistochemical stain), or Lef1 immunofluorescence (scale bars=100μm). See also Figure S4.

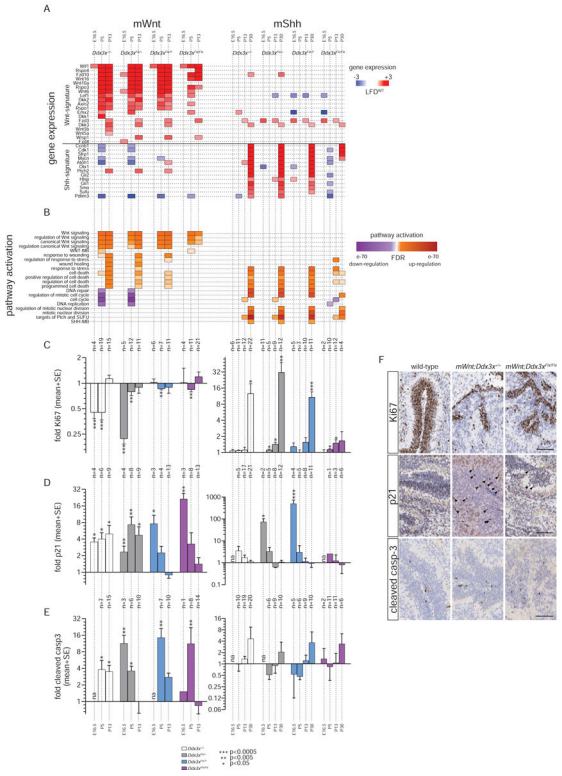

Figure 5. *Ddx3x* suppresses oncogenic Wnt-signaling in the developing cerebellum.

Heatmaps reporting the log-fold difference (LFD) in expression of the indicated genes (**A**) or False Discovery Rate of the indicated pathway up- or down-regulation (**B**) in premalignant cerebellar isolated from mice predisposed to develop either Wnt- (left) or Shh-medulloblastoma (right) harboring the indicated *Ddx3x* alleles at the indicated developmental time points relative to *Blbp-Cre*$^{+/-}$*;Ddx3x*$^{+/+}$ controls (≥5 cerebellar/genotype/time point). Fold change in Ki67 (**C**), p21 (**D**) and cleaved Caspase 3 (**E**) immunohistochemistry in the mice shown in (A and B) relative to *Blbp-Cre*$^{+/-}$*;Ddx3x*$^{+/+}$ controls (n≥10). The number 'n' of brains analyzed in each assay is shown above each bar. *=p<0.05; **=p<0.005; ***=p<0.0005, Mann-Whitney. **F.** Exemplary immunohistochemical stains in P5 cerebella of the indicated mice; scale bar = 50μm.

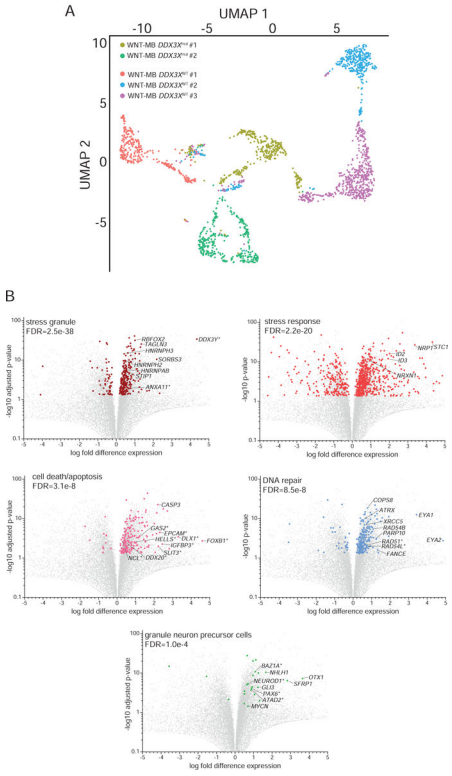

Figure 6. Single cell RNAseq of human *DDX3X*^{mut} and *DDX3X*^{wt} WNT-medulloblastoma.

A. UMAP of single cell RNAseq profiles generated from human *DDX3X*^{mut} (n=2) and *DDX3X*^{wt} (n=3) WNT-medulloblastoma. **B**. Volcano plots of -log10 p-values versus log fold difference expression of genes in the human *DDX3X*^{mut} and *DDX3X*^{wt} WNT-medulloblastomas in (A). Coloured genes in each plot belong to the cell pathway with associated FDR enrichment (top left). Exemplar genes are indicated; those marked with an asterix were also upregulated in mouse *Blpb-Cre*$^{+/-}$*;mWnt;Ddx3x*$^{Flx/Y}$ cerebella tumors. See also Figure 4C and S5.

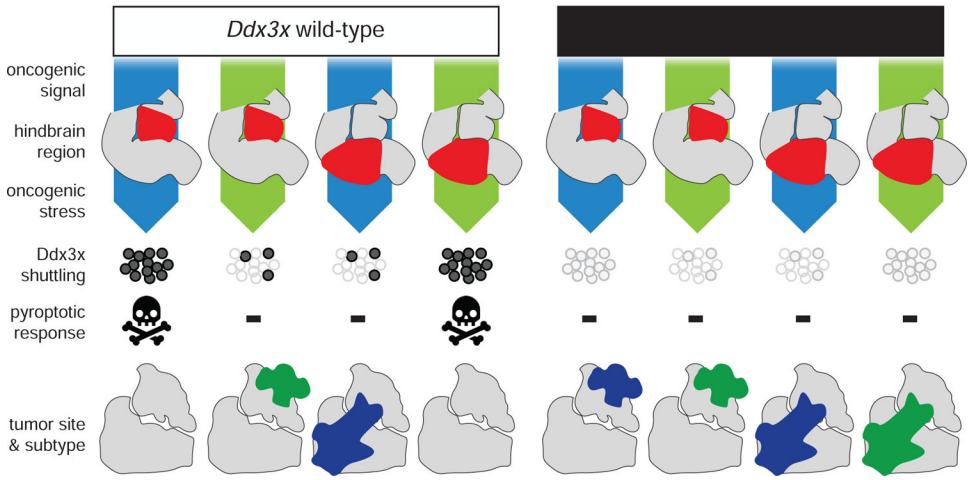

Figure 7. Cartoon depicting the proposed role of *Ddx3x* in sensing oncogenic stress signals in the hindbrain.

In the context of wild-type *Ddx3x* shown left, oncogenic Wnt and Shh-signals in the lower and upper rhombic lip, respectively are relatively well tolerated. This provokes only a modest oncogenic stress response and fails to trigger a major inflammasome-pyroptotic death signal, markedly increasing the probability of forming medulloblastoma. Conversely, activation of oncogenic Wnt and Shh-signals in the upper and lower rhombic lip, respectively in which they are not primary mitogens, provokes a massive pyroptotic and tumor suppressing response. In the context of mutant *Ddx3x* shown right, this tumor suppressing pyroptotic cell death response is lost, allowing Wnt and Shh-medulloblastomas to form in either the upper or lower rhombic lips.

KEY RESOURCES TABLE

REAGENT or RESOURCE	SOURCE	IDENTIFIER
Antibodies		
Donkey anti-Rabbit IgG, Alexa Fluor 488	Thermo Fisher Scientific	Cat# A-21206; RRID:AB 2535792
Donkey anti-Rabbit IgG, Alexa Fluor 564	Thermo Fisher Scientific	Cat# A-21207; RRID:AB 141637
Donkey anti-Rabbit IgG, Alexa Fluor 680	Thermo Fisher Scientific	Cat# A10043; RRID;AB 2534018
Goat polyclonal anti-Contactin2	R&D Systems	Cat# AF4439; RRID:AB 2044647
Mouse monoclonal anti-G3BP1	Proteintech	Cat# 66486-1-Ig; RRID:AB 2819031
Mouse monoclonal anti-NeuN	Millipore	Cat # MAB377; RRID:AB 2298772
Mouse monoclonal anti-p21	BD Biosciences	Cat# 556431; RRID:AB 396415
Mouse monoclonal anti- Synaptophysin	Cell Signaling	Cat# 9020; RRID:AB_2631095
Rabbit monoclonal anti-Cleaved Caspase-3	Cell Signaling	Cat# 9664; RRID:AB_2070042
Rabbit monoclonal anti-Irf1	Abcam	Cat# ab240299, RRID:AB 2737059
Rabbit monoclonal anti-Lef1	Abcam	Cat# ab137872; RRID:AB 1267233
Rabbit monoclonal anti-Mouse IgG	Abcam	Cat# ab6728; RRID:AB 955440
Rabbit polyclonal anti-Beta actin	Cell Signaling	Cat# 4967; RRID:AB 330288
Rabbit polyclonal anti-Calbindin	Millipore	Cat# AB1778; RRID:AB 2068336
Rabbit polyclonal anti-CD3	Agilent Dako	Cat# A0452, RRID:AB 2335677
Rabbit polyclonal anti-Ddx3x	Bethyl	Cat# A300–474A; RRID:AB 451009
Rabbit polyclonal anti-Gfap	Agilent Dako	Cat# Z0334; RRID:AB 10013382
Rabbit polyclonal anti-Iba1	Wako	Cat# 013–27691, RRID:AB 839504
Rabbit polyclonal anti-Ki67	Abcam	Cat# ab15580; RRID:AB 443209
Rabbit polyclonal anti-Ki67	Bethyl	Cat# IHC-00375; RRID:AB 1547959
Rabbit polyclonal anti-Pax-6	Biolegend	Cat# 901301; RRID:AB 2565003
Rat monoclonal anti-CD45	Abcam	Cat# ab25386, RRID:AB 470499
Rat monoclonal anti-CD68	Abcam	Cat# ab53444, RRID:AB 869007
Rat monoclonal anti-F4/80	Bio-Rad	Cat# MCA497, RRID:AB 2098196
Rat monoclonal anti-Ki67	Thermo Fisher Scientific	Cat# 14-5698-82; RRID:AB 10854564
IRDye 680LT Donkey anti rabbit IgG	LI-COR	Cat# 926-68023; RRID:AB 10706167
Bacterial and Virus Strains		
YFP-luciferase lentivirus	Mohankumar et al., 2015	NA
Cre-recombinase lentivirus	Tong et. al., 2015	NA
Biological Samples		
Mouse Cerebellum	This manuscript	NA
Mouse MB Tumours	This manuscript	NA
Chemicals, Peptides, and Recombinant Proteins		
Accutase	Thermo Fisher Scientific	Cat# A1110501
Acetic Acid	Sigma-Aldrich	Cat# A6283
B-27 Supplement	Thermo Fisher Scientific	Cat# 12587010

REAGENT or RESOURCE	SOURCE	IDENTIFIER
Collagenase Type IV	Thermo Fisher Scientific	Cat# 17104-019
Cresyl Fast Violet	Sigma-Aldrich	Cat# C5042
DAPI	Cell Signaling	Cat# 4083
Epitope Retrieval Solution 2	Leica Biosystems	Cat# AR9640
Eosin	Thermo Fisher Scientific	Cat# 7111
Hematoxylin	Thermo Fisher Scientific	Cat# 7221
Human EGF	MACS Miltenyi Biotec	Cat# 130-097-751
Human FGF-2	MACS Miltenyi Biotec	Cat# 130-093-843
Hyaluronidase	Sigma-Aldrich	Cat# H3757
iBlot™ Transfer Stack, nitrocellulose	Thermo Fisher Scientific	Cat# IB301001
Matrigel Matrix	Corning	Cat# 354230
N-2 Supplement	Thermo Fisher Scientific	Cat# A1370701
Neurobasal Medium	Thermo Fisher Scientific	Cat# 21103049
Normal Donkey Serum	Sigma-Aldrich	Cat# D9663
NuPAGE, 4–12% Bis-Tris protein gel	Thermo Fisher Scientific	Cat# NP0335
ProLong Gold antifade mountant	Thermo Fisher Scientific	Cat# P36930
Protease Inhibitors	Sigma-Aldrich	Cat# P8340
RIPA Lysis Buffer	Invitrogen	Cat# 89901
RNAscope® 2.5 LS Probe - Mm- Ddx3x	Advanced Cell Diagnostics	Cat# 490438
RNAscope® 2.5 LS Probe- Mm- Atoh1	Advanced Cell Diagnostics	Cat# 408798
RNAscope® 2.5 LS Probe- Mm- Gbx2	Advanced Cell Diagnostics	Cat# 314358
RNAscope® 2.5 LS Probe- Mm- Hoxa2	Advanced Cell Diagnostics	Cat# 451268
RNAscope® 2.5 LS Probe- Mm- Otx2	Advanced Cell Diagnostics	Cat# 444388
RNAscope® 2.5 LS Probe- Mm- Pax5	Advanced Cell Diagnostics	Cat# 311488
VectaMount Permanent Mounting Medium	Vector Laboratories	Cat# H-5000
Critical Commercial Assays		
Kapa qPCR library quantification kit	Kapa Biosystems	Cat# KK4873
TruSeq stranded mRNA kit	Illumina	Cat# 20020595
Leica Polymer Refine Detection System	Leica Biosystems	Cat# DS9800
Nextera Flex pre-enrichment kit	Illumina	Cat# 20025523
Polymer Refine Red Detection Kit	Leica Biosystems	Cat# DS9390
RNAscope® 2.5 LS Duplex Reagent Kit	Advanced Cell Diagnostics	Cat# 3224400
RNAscope® 2.5 LS Green Accessory Pack	Advanced Cell Diagnostics	Cat# 322550
RNeasy Plus universal kit	Qiagen	Cat# 73404
truXTRAC FFPE Total NA Plus Kit	Covaris	Cat# PN 520255
Deposited Data		
DNA sequencing data	This manuscript	GSE147069
RNA sequencing data	This manuscript	GSE147178
Experimental Models: Cell Lines		

REAGENT or RESOURCE	SOURCE	IDENTIFIER
Mouse: Ddx3x^{flx}	This manuscript	NA
Mouse: Blbp-Cre$^{+/-}$;Ctnnb 1 $^{+/lox(ex3)}$;Tp53 $^{+/flx}$	This manuscript	NA
Mouse: Blbp-Cre$^{+/-}$;Ddx3x$^{tlx/tlx}$;Ctnnb 1 $^{+/lox(ex3)}$;Tp53 $^{+/flx}$	This manuscript	NA
Experimental Models: Organisms/Strains		
Ddx3x^{flx}	Samir et. al. 2019	NA
Blbp-Cre$^{+/-}$; Ctnnb1$^{+/lox(ex3)}$;Tp53$^{+/tlx}$	Gibson et. al. 2010	NA
Blbp-Cre$^{+/-}$; Ddx3x^{flx}; Ctnnb$^{1+/lox(ex3)}$; Tp53$^{+/flx}$	This manuscript	NA
Ptch1^{tm1Hahn} (Ptch$^{+/-}$)	The Jackson Laboratory; Uhmann et. al. 2007	Stock# 012457 (RRID: IMSR_JAX:012457)
Blbp-Cre$^{+/-}$; Ddx3x^{flx}; Ptch$^{+/-}$	This manuscript	NA
CD1-Foxn1^{NU}	Charles River	Strain # 086; RRID:IMSR_CRL:086
Oligonucleotides		
Ddx3x Intron 6 forward primer	Integrated DNA Technologies	TTCTGGAGGCAATACTGGGA
Ddx3x Intron 6 reverse primer	Integrated DNA Technologies	ATGAGCTTACCTGTTTGAGCA
Ddx3x Intron 14 forward primer	Integrated DNA Technologies	CCGTGTGGGAAACCTTGGTA
Ddx3x Intron 14 reverse primer	Integrated DNA Technologies	AGAACGTCCACGACTGCTAC
Ptch forward primer	Integrated DNA Technologies	TTCATTGAACCTTGGGGAAC
Ptch reverse primer	Integrated DNA Technologies	AGTGCGTGACACAGATCAGC
Recombinant DNA		
Software and Algorithms		
Aperio ePathology	Leica Biosystems	www.leicabiosystems.com
Aperio ImageScope	Leica Biosystems	www.leicabiosystems.com
Burrows-Wheeler Aligner (BWA)	(Li and Durbin, 2010)	www.sourceforge.net/projects/bio-bwa/
CGHcall package (version 2.44.0)	(van de Wiel et al., 2007)	www.bioconductor.org/packages/release/bioc/html/CGHcall
DESeq2 package (version 1.26.0)	(Love et al., 2014)	www.bioconductor.org/packages/release/bioc/html/DESea2
DNAcopy package (version 1.56.0)	R package version 1.58.0	www.bioconductor.org/packages/release/bioc/html/DNAcopy
GraphPad Prism 6.00	GraphPad	www.graphpad.com
QDNAseq package (version 1.12.0)	(Scheinin et al., 2014)	www.bioconductor.org/packages/release/bioc/html/QDNAsea
Other		
Ultra-low attachment T75 flask	Corning	Cat# 3814